arXiv:cond-mat/9911008v1 [cond-mat.stat-mech] 2 Nov 1999

Theoretical study of collective modes in DNA at ambient temperature

Simona Cocco [1,2,3] and Rémi Monasson [3]

[1] *Dipartimento di Scienze Biochimiche, Università di Roma "La Sapienza", P.le A. Moro, 5 - 00185 Roma, Italy*

[2] *CNRS-Laboratoire de Physique de l'ENS-Lyon, 46 Allée d'Italie, 69364 Lyon Cedex 07, France.*

[3] *CNRS-Laboratoire de Physique Théorique de l'ENS, 24 rue Lhomond, 75005 Paris, France.*

The instantaneous normal modes corresponding to base pair vibrations (radial modes) and twist angle fluctuations (angular modes) of a DNA molecule model at ambient temperature are theoretically investigated. Due to thermal disorder, normal modes are not plane waves with a single wave number q but have a finite and frequency dependent damping width. The density of modes $\rho(\nu)$, the average dispersion relation $\nu(q)$ as well as the coherence length $\xi(\nu)$ are analytically calculated. The Gibbs averaged resolvent is computed using a replicated transfer matrix formalism and variational wave functions for the ground and first excited state. Our results for the density of modes are compared to Raman spectroscopy measurements of the collective modes for DNA in solution and show a good agreement with experimental data in the low frequency regime $\nu < 150$ cm^{-1}. Radial modes extend over frequencies ranging from 50 cm^{-1} to 110 cm^{-1}. Angular modes, related to helical axis vibrations are limited to $\nu < 25$ cm^{-1}. Normal modes are highly disordered and coherent over a few base pairs only ($\xi < 20\mathring{A}$) in good agreement with neutron scattering experiments.

I. INTRODUCTION

Much attention has been paid in the last twenty years to low frequency dynamics of DNA due to its relevance to biological processes. Vibrational modes involving collective motions of groups of atoms have been experimentally investigated by means of various techniques as neutron scattering [1–3], spectroscopy measurements [4–8], NMR, ... Among the latters, Raman studies carried out by H. Urabe *et al.* [5–7,9] have revealed particulary useful to gain information on the dependence of low frequency vibrations properties of DNA upon external conditions e.g. water content, ionic concentration, temperature. The observation of the Raman scattering intensity in the low frequency region is technically very difficult because the strong solvent Rayleigh scattering near zero frequency masks the DNA response. Nevertheless a broad band ranging from 60 cm^{-1} to 100 cm^{-1} has been evidenced and associated to hydrogen bonded base pair vibrations [5,6]. Moreover experiments focusing on oriented solid DNA fibers have also exhibit sharp peaks in the Raman intensity at $\simeq 16$ cm^{-1}, that shifts toward lower frequency region when rising the degree of hydration [7]. The origin of this peak is far from being obvious. In particular, its interhelical or intrahelical origine has been debated for a long time [9].

To reach a better understanding of the above experimental findings, detailed theoretical analysis of DNA vibrational motions have been proposed. Devoting a particular attention to hydrogen bond stretching modes, Prohofsky and his collaborators [10] have been able to find back a vibration mode at 85 cm^{-1} and confirm its origin. Their approach is based on a detailed description of the DNA molecule at the atomic level [11] and a variational calculation method, called modified self-consistent phonon approximation (MSPA). Within MSPA, the molecule at ambient temperature is reduced to an effective (and complex) harmonic lattice the force constants of which are determined in a self-consistent way. This approach has been very useful in calculating many properties of DNA, e.g. the melting of DNA's of different sequences [12], [13], the temperature and salt dependence of the B to Z conformation change [14] and the stability of drug-DNA complex [15].

A qualitative weakness of MSPA, that also arises in other simplified theoretical approaches [16] lies in the *a priori* nature of modes. Though effective elastic constants depends on temperature, normal modes indeed conserve a plane wave structure [10]. As a consequence, dispersion relations for the normal modes are well defined as for phonons in crystals [17]. In other words, the coherence length is infinite and the momentum selection rule give rise to a discrete set of lines in the theoretical predictions for Raman spectra [17]. On the contrary, amorphous materials or more generally thermally disordered systems give rise to normal modes with short coherence lengths, whose power spectrum displays a finite width [2,3,18]. As a result, momentum selection rules break down and light scattering processes may occur from essentially all normal modes [19,20]. Correspondingly for a DNA molecule in solution, the Raman spectrum is continuous and does not depend on the wave length of the incident laser beam nor on the scattering angle [5].

Understanding the vibrations of a system in presence of thermal (or configurational) disorder is a difficult task [21,22]. Non-harmonicities in the interactions between constituents may modify deeply the usual phonon picture of wave propagation in solids and generally forbid any rigorous analytical treatment of the dynamical equations. An interesting approach to circumvent this difficulty has been proposed in the context of liquid state dynamics [23]. The idea is to start from a randomly chosen configuration at thermodynamical equilibrium. Then, the equations of motion

around this fixed initial configuration can be linearized, defining some instantaneous normal modes (INM) and their corresponding relaxation times *i.e.* frequencies. All these quantities may then be averaged over the initial configuration chosen from the Gibbs ensemble at the desired temperature. One obtains this way a precise description of the short times dynamics based on the average spectrum of relaxation times and the statistical properties of the INM [23]. As a major advantage, the INM approach takes into account thermal disorder through the choice of the random initial configuration and gives rise to highly disordered normal modes with finite autocorrelation length as expected at finite temperature. Due to the linearization procedure, the information available through INM calculations is restricted to short times dynamics. This limitation is however not serious in the range of frequencies mentioned above for DNA collective dynamics as we shall see later.

From a theoretical point of view, the calculation of the INM around a fixed intial configuration is a hard task that can be performed analytically for simple enough models only [24–26]. In this paper we describe the torsional and hydrogen bond stretching vibrations of a very simple DNA model by normal modes that are not plane waves using the INM approach. We are able in particular to calculate the frequency dependent density of state at a given temperature, the coherence length of the normal modes and some pseudo dispersion relations at ambient temperature. The model that we consider has been introduced in a previous article to study the DNA denaturation driven by temperature or mechanically induced by a torque [27]. This study was motivated by the recent development of micromanipulation techniques [28,29] that have allowed the direct observation of DNA denaturation induced by an external torsional stress [30,31]. Our model describes the DNA molecule at the base pair level, and for each base pair we have just two degrees of freedom that is the base pair radius and twist angle. As a result, the potential energy is sufficiently simple to allow for sophisticated analytical calculations of normal collective modes. From a technical point of view, our calculation is inspired from a recent study of instantaneous modes in an one dimensional disordered system [32], that mixes techniques used in localization theory (the resolvent calculation), disordered system (replica trick) [33] and a variational Gaussian wave function method. As we shall see, the interest of the calculation is two-fold. First, it gives theoretical predictions for the spectrum of modes, the effective dispersion relations and damping width at ambient temperature that can be directly confronted with Raman spectroscopy and to neutron scattering data. Secondly, it is a way to check the validity of (and eventually improve) our model in very different experimental conditions from the the ones it was originally designed for.

The paper is organized as follows. In Section II, we define the DNA model and explain how to compute its statistical physics properties. The choice of the force constants and the main thermodynamical features are then exposed. Section III is devoted to dynamics and to the definiton of the instantaneous modes. The relationship between the latters and Raman spectra is evoked. The analytical framework necessary to calculation the properties of INM is presented in Section IV. Results are given and compared to experiments in Section V. Finally, we present some conclusions and perspectives in Section VI.

II. PRESENTATION AND MAIN FEATURES OF THE DNA MODEL

In this Section, we describe the DNA model under study and briefly recall how it can be studied using statistical mechanics techniques as well as its main thermodynamical features, see [27]. We then discuss the properties of the normal modes, e.g. dispersion relations, spectral density, ... of the molecule in the absence of temperature and interaction with the solvent.

A. Definition of the model

Our model reproduces the Watson-Crick double helix (B-DNA) as schematized fig 1. Each base pair ($j = 1, \ldots, N$) is described by its radius r_j and the angle φ_j in the plane perpendicular to the helical axis [34]. The sugar phosphate backbone is made of rigid rods, the distance between adjacent bases on the same strand being fixed to $L = 6.95\mathring{A}$. Conversely, the distance h_j between base planes $j-1$ and j is allowed to fluctuate. The Hamiltonian V associated to a configuration of the degrees of freedom $\{r_j, \varphi_j\}$ is the sum of three different contributions,

$$V[\{r_j, \varphi_j\}] = \sum_{j=1}^{N} V_m(r_j) + \sum_{j=2}^{N} \left(V_s(r_j, r_{j-1}) + V_b(r_j, r_{j-1}, \varphi_j - \varphi_{j-1})\right) \qquad , \tag{1}$$

that we now describe.

- Hydrogen bonds inside a given pair n are taken into account through the short-range Morse potential [10,35]

$$V_m(r_j) = D\,\left(e^{-a(r_j-R)}-1\right)^2 \tag{2}$$

with $R = 10\mathring{A}$. The width of the well amounts to $3a^{-1} \simeq 0.5\mathring{A}$ [36], in agreement with the order of magnitude of the relative motion of the hydrogen bonded bases [37]. A base pair with diameter $r > r_d = R + 6/a$ may be considered as open. The potential depth D, typically of the order of $0.1eV$ [10] depends on the base pair type (Adenine-Thymine (AT) or Guanine-Citosine (GC)) as well as on the ionic strength. Note that the Morse potential V_m increases exponentially with decreasing $r < R$ and may be considered as infinite for $r < r_{min} = 9.7\mathring{A}$ [38].

- The shear force that opposes sliding motion of one base over another in the B-DNA conformation is accounted for by the stacking potential [39]

$$V_s(r_j, r_{j-1}) = E\, e^{-b(r_j+r_{j-1}-2R)}\,(r_j - r_{j-1})^2 \qquad . \tag{3}$$

  Due to the decrease of molecular packing with base pair opening, the shear prefactor is exponentially attenuated and becomes negligible beyond a distance $\simeq 5b^{-1} = 10\mathring{A}$, which coincides with the diameter of a base pair [36].

- An elastic energy is introduced to describe the vibrations of the molecule in the B phase,

$$\begin{aligned} V_b(r_j, r_{j-1}, \theta_j) &= K\big(h_j - H\big)^2 \\ &= K\left(\sqrt{L^2 - r_j^2 - r_{j-1}^2 + 2r_j r_{j-1}\cos\theta_j} - H\right)^2 \end{aligned} \tag{4}$$

  where $\theta_j = \varphi_j - \varphi_{j-1}$ is the twist angle between base pairs $j-1$ and j. The helicoidal structure arises from the choice of $H < L$: in the rest configuration $r_j = R$ at $T = 0$K, V_b is minimum and zero for the twist angle $\Theta > 0$ with $\sin(\Theta/2) = \sqrt{L^2 - H^2}/(2R)$. The above definition of V_b holds as long as the argument of the square root in (4) is positive, that is if r_j, r_{j-1}, θ_j are compatible with rigid rods having length L. By imposing $V_b = \infty$ for negative arguments, unphysical values of r_j, r_{j-1}, θ_j are excluded. As the behaviour of a single strand ($r > r_d$) is uniquely governed by this rigid rod condition, the model does not only describe vibrations of helicoidal B-DNA but is also appropriate for the description of the denaturated phase [27].

B. Calculation of partition function

The configurational partition function at inverse temperature $\beta = 1/(k_B T)$ reads

$$Z = \int_{r_{min}}^{\infty} r_1 dr_1 \int_{-\infty}^{\infty} d\varphi_1 \ldots \int_{r_{min}}^{\infty} r_N dr_N \int_{-\infty}^{\infty} d\varphi_N \;\exp\Big\{-\beta V[\{r_j,\varphi_j\}]\Big\}\,\delta(\varphi_1)\prod_{j=2}^{N}\chi\big(\theta_j\big)\;. \tag{5}$$

The angle of the first extremity of the molecule is set to $\varphi_1 = 0$ with no restriction (due to the arbitrary choice of the angular reference axis, see fig 1) whereas the last one φ_N is not constrained. The χ factors entering (5) are defined by $\chi(\theta_j) = 1$ if $0 \le \theta_j = \varphi_j - \varphi_{j-1} \le \pi$ and 0 otherwise to prevent any clockwise twist of the chain. Partition function Z can be calculated using the transfer integral method [40],

$$Z = \int_{r_{min}}^{\infty} r_1 dr_1 \int_{r_{min}}^{\infty} r_N dr_N \int_{-\infty}^{\infty} d\varphi_N \;\langle r_N, \varphi_N | T^N | r_1, 0\rangle \quad , \tag{6}$$

where the transfer operator entries read $\langle r, \varphi | T | r', \varphi'\rangle = T(r, r', \theta)$ with $\theta = \varphi - \varphi'$ and

$$T(r, r', \theta) = X(r, r')\,\exp\left\{-\beta V_b\left(r, r', \theta\right)\right\}\,\chi\big(\theta\big) \quad , \tag{7}$$

$$X(r, r') = \sqrt{rr'}\;\exp\left\{-\frac{\beta}{2}\left(V_m\left(r\right) + V_m\left(r'\right)\right) - \beta V_s\left(r, r'\right)\right\} \qquad . \tag{8}$$

At fixed r, r', the angular part of the transfer matrix T is translationally invariant in the angle variables φ, φ' and can be diagonalized through a Fourier transform. Thus, for each Fourier mode k we are left with an effective transfer matrix on the radius variables

$$T_k(r,r') = X(r,r')\, Y_k(r,r') \tag{9}$$

with

$$Y_k(r,r') = \int_0^\pi d\theta \exp\Big\{ -\beta V_b\,(r,r',\theta) - ik\theta \Big\} \quad . \tag{10}$$

The only mode contributing to Z is $k=0$ once φ_N has been integrated out in (5). In the $N \to \infty$ limit, the free-energy density f is simply given by $f = -k_B T \ln \lambda_0$, where λ_0 is the maximal eigenvalue of T_0 whose corresponding eigenvector will be denoted by $\psi_0(r)$.

C. Thermodynamical properties and parameters

The ground state wave function $\psi_0(r)$ is shown figure 2 at ambient temperature $T = 300$ K. It is entirely localized in the Morse potential well as expected for a DNA molecule in B configuration. The first excited eigenstate of the transfer matrix has an excess free-energy ΔG with respect to ψ_0 and is delocalized: it extends over all values of $r > r_d$, vanishes for $r < r_d$ and thus represents a denaturated molecule. At some higher temperature T_m, the bound wave function disappears and ψ_0 suddenly undergoes a delocalization transition. In other words, hydrogen bonds break up and T_m can be interpreted as the melting temperature [27].

The values of the parameters entering the potential energy is discussed in [27] and are listed below:

- inverse hydrogen bond length: $a = 6.3 \mathring{A}^{-1}$.
- zero temperature interplane distance: $H = 3\mathring{A}$.
- Morse potential depth: $D = 0.16eV$.
- attenuation coefficient for stacking interactions: $b = 0.49 \mathring{A}^{-1}$.
- stacking stiffness: $E = 4eV/\mathring{A}^2$.
- backbone elasticity constant: $K = 0.014eV/\mathring{A}^2$.

The values of a and b have been borrowed from literature [27]. The choice of the other parameters D, E, K, H ensures that geometrical and thermodynamical properties as the average twist angle, the mean axial distance between successive bases in the B conformation, the melting temperature $T_m = 350$ K and the denaturation free-energy ΔG are correctly predicted [27].

Notice that the main uncertainty in this tuning procedure arise with the choice of the stacking stiffness E. Three possible pairs of parameters (D, E) that correctly fit $T_m = 350$ K are listed in Table A 4, as well as the corresponding denaturation free-energies ΔG at $T = 300$ K. We have selected the pair giving the largest prediction for the denaturation free-energy that is in closest agreement with thermodynamical estimates of ΔG [39]. It can be easily seen from Table A 4 that E varies much more than D and ΔG and is therefore less accurately predicted than the other parameters of the model.

III. DYNAMICS AND INSTANTANEOUS NORMAL MODES

Our aim is to perform an analytical calculation of the spectrum of torsional and radial vibrations on characteristic time scale of the pico seconds and at ambient temperature. In this section, we first write the dynamical equations for the model. We then linearize these equations around a given (and randomly chosen) configuration of the thermally equilibrated system and define the instantaneous normal modes as the vibrations of the DNA molecule around this configuration. The density of instantaneous normal modes can be related to some extent to the Raman intensity. Finally, we consider the special case of zero temperature. The explicit calculation of the dispersion relations and the density of modes allows for a decoupling of the angular and radial motions. It will also provides useful comparisons with the finite temperature results of Section V.

A. Dynamical equations for the DNA model

We denote the configuration of the molecule at time t by $\{r_j^t, \varphi_j^t\}$. The equations of motion read

$$\begin{aligned} m\,\ddot{r}_j^t &= m\,r_j^t(\dot{\varphi}_j^t)^2 - \frac{1}{2}\frac{\partial V}{\partial r_j^t} \\ m\,(r_j^t)^2\ddot{\varphi}_j^t &= -\frac{1}{2}\frac{\partial V}{\partial \varphi_j^t} \quad , \end{aligned} \tag{11}$$

where the potential energy V has been defined in (1). The effective half mass $m = 300$ u.m.a. of a base pair takes into account the atomic consituents of the nucleotide and of the backbone as well as the primary hydration shell which is tightly bound to the base [16,39,41]. The size of the primary shell depends on the hydration degree and is of the order of 10-20 water molecules per nucleotide. The characteristic relaxation time of the primary shell is typically $\tau_1 \simeq 10^{-10}$ s [41]. Therefore, for dynamical processes taking place on time scales $\tau < \tau_1$, that is for frequencies $\nu > 0.3$ cm^{-1} primary shells may be considered as rigidly linked to the bases and simply taken into account through the effective mass m. Our choice for m is in close agreement with the mass considered by Volkov and Kosevich [42]. Taking into the additional water shell mass and averaging over the possible bases A,T,G and C, these authors have calculated somes estimates of the masses of the nucleotide $m_n = 199$ u.m.a. and of the backbone elements $m_b = 109$ u.m.a. giving a total mass $m = m_n + m_b = 308$ u.m.a. per base [42].

The secondary hydration shell contains less rigidly bound water molecules that induce some friction acting on the DNA molecule. The characteristics scale time of viscosity dissipation at ambient temperature is $\tau_2 \simeq 10^{-12}$ s [41,43], that is of the same order of magnitude as in bulk water. The viscous terms $-\gamma\,\dot{r}_j^t$ and $-\gamma\,\dot{\varphi}_j^t$ that should be included in the motion equations (11) can be neglected on time scales $\tau < \tau_2$ that is for frequencies $\nu > 30$ cm^{-1} only. In the following we shall use the non dissipative equations (11) keeping in mind that the interpretation of the results must be made with care for frequencies smaller than 30 cm^{-1}.

B. Linearization approximation and instantaneous modes

We linearize the equations of motions (11) around a casual initial configuration $\mathcal{C} = \{r_j, \varphi_j\}$ of the system already in thermodynamical equilibrium, defining for each base pair j,

$$\begin{aligned} r_j^t &= r_j + y_j^t \\ \varphi_j^t &= \varphi_j + \tilde{\phi}_j^t. \end{aligned} \tag{12}$$

Once linearized the dynamical equations (11) are rewritten in terms of the displacement variables $y_j^t, \phi_j^t \equiv R.\tilde{\phi}_j^t$ and read

$$\begin{aligned} m\,\ddot{y}_j^t &= \sum_k (\mathcal{D}_r^{\mathcal{C}})_{j,k}\,y_k^t + \sum_k (\mathcal{D}_m^{\mathcal{C}})_{j,k}\,\phi_k^t \\ m\,\ddot{\phi}_j^t &= \sum_k (\mathcal{D}_m^{\mathcal{C}})_{k,j}\,y_k^t + \sum_k (\mathcal{D}_\varphi^{\mathcal{C}})_{j,k}\,\phi_k^t \end{aligned} \tag{13}$$

where

$$\left(\mathcal{D}_r^{\mathcal{C}}\right)_{jk} = \frac{1}{2}\frac{\partial^2 V}{\partial r_j \partial r_k}\bigg|_{\mathcal{C}} \quad , \qquad \left(\mathcal{D}_m^{c}\right)_{jk} = \frac{1}{2R}\frac{\partial^2 V}{\partial r_j \partial \varphi_k}\bigg|_{\mathcal{C}} \quad \text{and} \qquad \left(\mathcal{D}_\varphi^{c}\right)_{jk} = \frac{1}{2R^2}\frac{\partial^2 V}{\partial \varphi_j \partial \varphi_k}\bigg|_{\mathcal{C}} \tag{14}$$

are the $N \times N$ matrices of second derivatives of the potential energy V around configuration $\mathcal{C}$. To solve the linear system (13) one has to find the eigenvalues λ of the $2N \times 2N$ Hessian matrix

$$\mathcal{D}^{\mathcal{C}} = \begin{pmatrix} \mathcal{D}_r^{\mathcal{C}} & \mathcal{D}_m^{\mathcal{C}} \\ \mathcal{D}_m^{\mathcal{C}} & \mathcal{D}_\varphi^{\mathcal{C}} \end{pmatrix} \quad . \tag{15}$$

It is important to notice that due to the dependence on the initial configuration $\mathcal{C}$ the elements of the matrix $\mathcal{D}^{\mathcal{C}}$ are not translationally invariant. Consequently, the eigenvectors of $\mathcal{D}^{\mathcal{C}}$, *i.e.* the instantaneous normal modes corresponding to the initial configuration $\mathcal{C}$ are not plane waves.

The eigenvalues histogram $\rho^{\mathcal{C}}(\lambda)$ give the density of the normal modes as a function of the initial configuration. The latter is distributed according to the Gibbs measure

$$\mathcal{P}(\mathcal{C} = \{r_j, \varphi_j\}) = \frac{1}{Z} \exp\left(-\beta V[\{r_j, \varphi_j\}]\right), \tag{16}$$

where V is the Hamiltonian defined in equation (1). Once averaged over distribution (16), the mean density of states $\rho(\lambda)$ is available and depends only on the temperature $T = 1/\beta$. The frequency spectrum $\rho_f(\nu)$ is straightforwardly obtained through the relationship, see (13),

$$\begin{aligned} \nu &= \frac{1}{2\pi}\sqrt{\frac{\lambda}{m}} \\ \rho_f(\nu) &= 4\pi\sqrt{m\,\lambda}\,\rho(\lambda) \qquad . \end{aligned} \tag{17}$$

To lighten notation, we shall drop the f subscript in (17) and use indifferently the same letter ρ to denote the density of states as a function of the eigenvalue λ or frequency ν.

The spectrum of the Hessian matrix (15) is not necessarily positive. Some instantaneous modes may be unstable and grow with time within the linear approximation. Their corresponding eigenvalues λ are negative and the associated frequencies ν are purely imaginary. Following the conventions of [23], imaginary frequencies ν will be conveniently represented by minus their modulus $-|\nu|$, that is by points on the negative frequency semi-axis. We shall come back in Section V to these modes.

C. Relationship with Raman spectra

In disordered solids the Raman scattering intensity is directly related to the density of normal modes. Indeed when the coherence length of the normal modes is short compared to optical wavelengths the conservation of momentum is no longer a restrictive selection rule and does not give rise to a discrete set of lines for the spectrum. Light scattering processes occur from essentially all the normal modes of the material and the spectra are continuous. As we will see later, the assumption of short coherence length is well verified in our model at finite temperature. The relationship between the Raman intensity $\mathcal{I}(\nu)$ and the density of normal modes $\rho(\nu)$ is generally expressed via the light-to-vibrations coupling coefficient $C(\nu)$ [19],

$$\mathcal{I}(\nu) = \rho(\nu)\, C(\nu)\, \left(\frac{n(\nu)+1}{\nu}\right) \qquad , \tag{18}$$

where

$$n(\nu) = \frac{1}{\exp\left(\frac{h\nu}{k_B T}\right) - 1} \tag{19}$$

is the average population of level ν. The spectral dependence of $C(\nu)$ is still an unsettled question. Early studies devoted to the relationship between Raman spectra and densities of modes assumed that the light-to-vibrations coupling was indepent of frequency, *i.e.* $C(\nu) = 1$ [19]. Later works conjectured a quadratic behaviour $C(\nu) \sim \nu^2$ at very low frequencies and a less steep increase for larger ν [20]. Recently, comparisons between neutron scattering experiments and calorimetric measures have given evidence for a linear dependence $C(\nu) \propto \nu$ for different glasses in the frequency range $8\,cm^{-1} < \nu < 100\,cm^{-1}$ [44,45], the upper bound being related to the Debye frequencies of the corresponding crystals.

D. Normal modes at zero temperature

The linearized equations af motions at zero temperature are obtained performing an expansion of the potential energy V up to the second order atound the rest positions: $r_j^t = R + y_j^t$, $\varphi_j^t = n\Theta + \phi_j^t/R$:

$$\begin{aligned} m\,\ddot{y}_j^t &= -a^2 D y_j^t - K_{yy}\left(2y^t{}_j + y^t{}_{j+1} + y^t{}_{j-1}\right) - E\left(2y_j^t - y_{j+1}^t - y_{j-1}^t\right) - K_{y\,\phi}\left(\phi_{j+1}^t - \phi_{j-1}^t\right) \\ m\ddot{\phi}_j^t &= -K_{\phi\phi}\left(2\phi_j^t - \phi_{j+1}^t - \phi_{j-1}^t\right) + K_{y\,\phi}\left(y_{j+1}^t - y_{j-1}^t\right) \end{aligned} \tag{20}$$

where

$$K_{yy} = \left(KR_0^2/H^2\right)(1-\cos\Theta)^2 \ , \tag{21}$$

$$K_{\phi\phi} = \left(KR_0^2/H^2\right)(\sin^2\Theta_0) \ , \tag{22}$$

$$K_{y\phi} = \left(KR_0^2/H^2\right)(\sin\Theta_0)(1-\cos\Theta_0) \tag{23}$$

The plane waves

$$\begin{pmatrix} y_j \\ \phi_j \end{pmatrix} = \begin{pmatrix} y_\pm(q) \\ \phi_\pm(q) \end{pmatrix} \exp\left\{i(qn - 2\pi\nu_\pm(q)t)\right\} \tag{24}$$

are solutions of (20) with the relations of dispersion $\nu_\pm(q)$ showed in fig 3. Due to the difference of the order of magnitude between $a^2D = 6.33\ eV\ \mathring{A}^{-2}$, $E = 4\ eV\ \mathring{A}^{-2}$ (or for the other choice of the parameters $a^2D = 5.93\ eV\ \mathring{A}^{-2}$, $E = 0.74\ eV\ \mathring{A}^{-2}$) and $K_{y\phi} = 18\ 10^{-3}\ eV\ \mathring{A}^{-2}$, $K_{yy} = 6\ 10^{-3}\ eV\ \mathring{A}^{-2}$, $K_{\phi\phi} = 54\ 10^{-3}\ eV\ \mathring{A}^{-2}$, it is clear that the angular and radial motions take place on two different time scales and become independent. The dispersion relations obtained when setting $K_{y\phi} = 0$ and $K_{yy} = 0$ are indistinguishable from the previous ones and read

$$\nu_r(q) \equiv \nu_+ = \frac{1}{2\pi}\sqrt{\frac{a^2D}{m} + 2\,\frac{E}{m}(1-\cos q)} \tag{25}$$

$$\nu_\varphi(q) \equiv \nu_- = \frac{1}{2\pi}\sqrt{\frac{2K_{\phi\phi}}{m}(1-\cos q)} \tag{26}$$

The density of states $\rho(\nu) = 1/(2\pi|\nu'(q)|)$ for each branch is given by

$$\rho_r(\nu) = \frac{4\pi\nu}{\sqrt{\left[(2\pi\nu)^2 - \frac{a^2D}{m}\right]\left[\frac{a^2D+4E}{m} - (2\pi\nu)^2\right]}} \tag{27}$$

$$\rho_\varphi(\nu) = \frac{1}{\sqrt{\frac{K_{\phi\phi}}{m} - (\pi\nu)^2}} \quad . \tag{28}$$

Note that the above densities are both normalized to 1/2 so that the total density of states $\rho_r(\nu) + \rho_\varphi(\nu)$ is properly normalized to unity. As shown fig 4, Van Hove singularities are located at frequencies ν such that the denominators in (28) vanish, that is stationary points of the dispersion relations (26).

E. Structure of the Hessian matrix

From the above considerations on the effective decoupling of radial and torsional modes, $\mathcal{D}_m^{\mathcal{C}}$ will be set to zero hereafter. Therefore, the Hessian matrix (15) is comprised of two $N \times N$ matrices, that is the radial Hessian matrix $\mathcal{D}_r^{\mathcal{C}}$ and the angular Hessian matrix $\mathcal{D}_\varphi^{\mathcal{C}}$. In what follows, the notation $\mathcal{D}^{\mathcal{C}}$ will generically refer to either of these two matrices.

Because only nearest neighbors along the molecule interact with each other, the Hessian matrix has a band diagonal structure,

$$(\mathcal{D}^{\mathcal{C}})_{kj} = \begin{cases} \frac{1}{2}d_0(r_j, r_{j-1}, \theta_j) + \frac{1}{2}d_0(r_j, r_{j+1}, -\theta_{j+1}) & \text{if} \quad k = j \\ -\frac{1}{2}d_1(r_j, r_{j-1}, \theta_j) & \text{if} \quad k = j-1 \\ -\frac{1}{2}d_1(r_{j+1}, r_j, \theta_{j+1}) & \text{if} \quad k = j+1 \\ 0 & \text{if} \quad |k-j| \geq 2 \end{cases} \quad . \tag{29}$$

Explicit expressions of elements d_0 and d_1 are:

- for the radius Hessian matrix $\mathcal{D}_r^{\mathcal{C}}$, the elements

$$\begin{aligned} d_0(r, r') &= \frac{1}{2}\frac{d^2V_m}{dr^2}(r) + 2E \quad , \\ d_1(r, r') &= 2E \quad , \end{aligned} \tag{30}$$

do not depend on the twist θ. For simplicity, we have not considered the exponential attenuation term in V_s which is almost constant (and equal to unity) in the B-DNA phase. K_{yy} has been set to zero since it is three orders of magnitude smaller than other radial force constants.

- for the twist Hessian matrix $\mathcal{D}^{\mathcal{C}}_{\varphi}$,

$$d_0(r,r',\theta) = d_1(r,r',\theta) = \frac{1}{R^2}\,\frac{d^2V_b}{d\theta^2}(r,r',\theta) \qquad , \tag{31}$$

where the backbone potential has been defined in (4).

IV. ANALYTICAL FRAMEWORK

A. Definition of spectral quantities

We call $\lambda^{\mathcal{C}}_e$ (respectively $w^{\mathcal{C}}_{a,e}$) the eigenvalues (respectively the components of the associated eigenvectors normalized to unity) of $\mathcal{D}^{\mathcal{C}}$, with $e = 1,\ldots,N$. Most spectral properties of $\mathcal{D}^{\mathcal{C}}$ can be obtained through the calculation of the resolvent [33]

$$G^{\mathcal{C}}_{ab}(\lambda + i\epsilon) = \left((\lambda + i\epsilon)\mathcal{I} - \mathcal{D}^{\mathcal{C}}\right)^{-1}_{ab} = \sum_{e=1}^{N} \frac{w^{\mathcal{C}}_{a,e} w^{\mathcal{C}}_{b,e}}{\lambda - \lambda^{\mathcal{C}}_e + i\epsilon} \qquad , \tag{32}$$

where $\mathcal{I}$ denotes the identity operator.

Introducing the density of eigenvalues

$$\rho^{\mathcal{C}}(\lambda) = \frac{1}{N}\sum_{e=1}^{N} \delta(\lambda - \lambda^{\mathcal{C}}_e) \qquad , \tag{33}$$

we may rewrite the discrete sum over eigenstates e in (32) as an integral over eigenvalues with measure $\rho^{\mathcal{C}}$. The knowledge of the trace of the resolvent,

$$\frac{1}{N}\sum_{a=1}^{N} G^{\mathcal{C}}_{aa}(\lambda + i\epsilon) = \frac{1}{N}\sum_{e=1}^{N} \frac{1}{\lambda - \lambda^{\mathcal{C}}_e + i\epsilon} = \int_{-\infty}^{\infty} d\mu\, \frac{\rho^{\mathcal{C}}(\mu)}{\lambda - \mu + i\epsilon} \quad , \tag{34}$$

gives then access to the density of states through identity

$$\rho^{\mathcal{C}}(\lambda) = -\frac{1}{\pi}\lim_{\epsilon\to 0^+} \mathrm{Im}\left[\frac{1}{N}\sum_{a=1}^{N} G^{\mathcal{C}}_{aa}(\lambda + i\epsilon)\right] \qquad . \tag{35}$$

Another quantity of interest is the autocorrelation function of eigenvectors at distance d,

$$A^{\mathcal{C}}_e(d) = \sum_{a=1}^{N-d} w^{\mathcal{C}}_{a,e} w^{\mathcal{C}}_{a+d,e} \qquad . \tag{36}$$

We then define $A^{\mathcal{C}}(\lambda, d)$ as the average value of $A^{\mathcal{C}}_e(d)$ over all eigenvectors e lying in the range $\lambda \le \lambda^{\mathcal{C}}_e \le \lambda + d\lambda$. This autocorrelation function is simply related to the off-diagonal resolvent (32) through

$$\frac{1}{N}\sum_{a=1}^{N-d} G^{\mathcal{C}}_{a,a+d}(\lambda + i\epsilon) = \int_{-\infty}^{\infty} d\mu\, \frac{\rho^{\mathcal{C}}(\mu)}{\lambda - \mu + i\epsilon}\, A^{\mathcal{C}}(\mu, d) \qquad , \tag{37}$$

that generalizes equation (34) to non zero values of d. Taking the imaginary part of equation (37), we obtain

$$\rho^{\mathcal{C}}(\lambda)\, A^{\mathcal{C}}(\lambda, d) = -\frac{1}{\pi}\lim_{\epsilon\to 0^+} \mathrm{Im}\left[\frac{1}{N}\sum_{a=1}^{N-d} G^{\mathcal{C}}_{a,a+d}(\lambda + i\epsilon)\right] \qquad . \tag{38}$$

Therefore, the calculation of the large distance d behaviour of $G^{\mathcal{C}}_{a,a+d}(\lambda + i\epsilon)$ will give access to the asymptotic scaling of the autocorrelation function

$$A^{\mathcal{C}}(\lambda, d) \propto \left(e^{-\sigma^{\mathcal{C}}(\lambda) + i\, q^{\mathcal{C}}(\lambda)}\right)^d \qquad , \tag{39}$$

and thus to some effective relation of dispersion $\lambda^{\mathcal{C}}(q)$ and to the coherence length $1/\sigma^{\mathcal{C}}(\lambda)$ of the instantaneous modes at finite temperature.

B. Average over the instantaneous molecular configuration

To perform the average over the molecule configurations $\mathcal{C}$, we first rewrite the resolvent (32) as the propagator of a replicated Gaussian field theory [33]

$$G^{\mathcal{C}}_{ab}(\lambda+i\epsilon) = \frac{-i\int\prod_{j=1}^N dx_j (x_a\, x_b)\ \exp\left(\frac{i}{2}(\lambda+i\epsilon)\sum_{j=1}^N {x_j}^2 - \frac{i}{2}\sum_{j,k=1}^N \mathcal{D}^{\mathcal{C}}_{j,k}\ x_j\, x_k\right)}{\int\prod_{j=1}^N dx_j\ \exp\left(\frac{i}{2}(\lambda+i\epsilon)\sum_{j=1}^N {x_j}^2 - \frac{i}{2}\sum_{jk=1}^N \mathcal{D}^{\mathcal{C}}_{jk}\ x_j\, x_k\right)}$$
$$= \lim_{n\to 0} -\frac{i}{n}\int\prod_{j=1}^N d\vec{x}_j (\vec{x}_a.\vec{x}_b)\ \exp\left(\frac{i}{2}(\lambda+i\epsilon)\sum_{j=1}^N {\vec{x}_j}^2 - \frac{i}{2}\sum_{j,k=1}^N \mathcal{D}^{\mathcal{C}}_{jk}\ \vec{x}_j.\vec{x}_k\right) \tag{40}$$

Replicated fields $\vec{x}_j = (x_j^1,\ldots,x_j^n)$ are n-dimensional vector fields attached to each site j. The positivity of ϵ ensures that the Gaussian integrals in (40) are well defined.

At equilibrium, the molecular configuration $\mathcal{C}$ is drawn according to the Gibbs measure (16). We shall denote the average of any quantity over distribution (16) in the same way as its configuration dependent counterpart but without $\mathcal{C}$ subscript. For instance, the average resolvent reads

$$G_{ab}(\lambda+i\epsilon) = \int_{r_{min}}^\infty r_1 dr_1 \int_{-\infty}^\infty d\varphi_1 \ldots \int_{r_{min}}^\infty r_N dr_N \int_{-\infty}^\infty d\varphi_N\ \mathcal{P}(\{r_j,\varphi_j\})\ G_{ab}^{\{r_j,\varphi_j\}}(\lambda+i\epsilon)\ , \tag{41}$$

where $\mathcal{P}$ is the Gibbs measure (16). It is important to keep in mind that $\mathcal{D}^{\mathcal{C}}_{jk}$ vanishes for $|j-k|\geq 2$, see Section III.2. Therefore, only replicated variables $\vec{x}_j, \vec{x}_k$ corrsponding to adjacent base pairs along the molecule ($j = k\pm 1$) interact together in the expression (40) of the resolvent.

C. Transfer matrix formalism

The one dimensional structure of the interactions in (41) can be exploited through the introduction of a transfer matrix $\mathcal{T}$ relating the molecular variables r_j, φ_j as well as the replicated variables $\vec{x}_j$ to their counterparts at site $j-1$. The entries of this matrix can be read from (1,40,41),

$$\langle r,\varphi,\vec{x}|\mathcal{T}|r',\varphi',\vec{x}'\rangle = T(r,r',\theta)\ \exp\left(\frac{i}{4}(\lambda+i\epsilon)(\vec{x}^2+\vec{x}'^2) - \frac{i}{4}d_0(r,r',\theta)\vec{x}^2\right.$$
$$\left. -\frac{i}{4}d_0(r',r,-\theta)\vec{x}'^2 + \frac{i}{2}\ d_1(r,r',\theta)\vec{x}.\vec{x}'\right) \quad . \tag{42}$$

In the above expression, d_0 and d_1 are respectively the diagonal and off-diagonal elements of $\mathcal{D}^{\mathcal{C}}$, see (29) while T has been defined in (8). Notice that $\mathcal{T}$ is a symmetric (but not Hermitian) matrix.

By definition, the average resolvent G_{ab} is the correlation function of replicated variables $\vec{x}_a$ and $\vec{x}_b$ (40). Within the transfer matrix formalism, this mean dot product can be computed from the knowledge of eigenvalues Λ_ℓ and all (normalized) eigenvectors $\Psi_\ell(r,\varphi,\vec{x})$ of $\mathcal{T}$. Calling d the axial distance $|a-b|$ between sites a and b along the molecule, the average resolvent reads in the thermodynamical limit

$$G_{ab}(\lambda+i\epsilon) = \lim_{n\to 0} -i\sum_{\ell=0}^\infty \left(\frac{\Lambda_\ell}{\Lambda_0}\right)^d \left[\int d\vec{x}\ dr\ d\varphi\ x^1\ \Psi_0(r,\varphi,\vec{x})\ \Psi_\ell(r,\varphi,\vec{x})\right]^2 \tag{43}$$

The maximal eigenvalue (in modulus) of $\mathcal{T}$ coincides with $\ell=0$ and increasingly excited states correspond to $\ell\geq 1$.

The average diagonal resolvent G_{aa} and thereby the mean density of states may be obtained from (43) when $d=0$,

$$\rho(\lambda) = \frac{1}{\pi}\lim_{\epsilon\to 0^+, n\to 0} \mathrm{Re}\left[\int d\vec{x}\ dr\ d\varphi\ \Psi_0(r,\varphi,\vec{x})^2\ (x^1)^2\right] \quad . \tag{44}$$

Expression (43) may also be used to compute the autocorrelation function of eigenvectors at large distances d. for which the resolvent (41) scale asymptotically as, see (39),

$$G_{a,a+d}(\lambda+i\epsilon) \propto \exp(-\sigma(\lambda)\ d + i\ q(\lambda)\ d) \qquad , \tag{45}$$

where both $\sigma(\geq 0)$ and q depend on the energy level λ. When d is large, the sum in (43) is dominated by the $\ell = 1$ contribution and equation (45) may be reformulated as

$$\lim_{d\to\infty} \frac{1}{d} \ln G_{a,a+d}(\lambda + i\epsilon) = -\sigma(\lambda) + i\, q(\lambda) \tag{46}$$

$$= \ln\left(\frac{\Lambda_1}{\Lambda_0}\right) \qquad , \tag{47}$$

which allows to derive σ and q from the knowledge of Λ_0 and Λ_1. We shall explicitely compute the inverse length σ and wave number q in Section V and compare them to the zero temperature results of Section II.D.

Notice that σ and q defined in (45) do not exactly coincide with the values of $\sigma^{\mathcal{C}}$ and $q^{\mathcal{C}}$ appearing in (39) averaged over $\mathcal{C}$ with distribution (16). To obtain the latter, one should average the logarithm of the resolvent $G^{\mathcal{C}}$ (quenched average) and not simply compute the logarithm of the mean resolvent as in (46) (annealed average) [46]. Due to concavity of the logarithm function, σ defined in (46) is not only a approximation but also a lower bound to the average value of $\sigma^{\mathcal{C}}$. Comparison with numerical simulations made for the so-called "smallworld" lattice have shown that σ provides a very good estimate of the mean $\sigma^{\mathcal{C}}$ [32]. To sum up, we can compute from the average resolvent G an upper bound $1/\sigma$ to the coherence length of the eigenvectors at level λ as well as an estimate q of their typical wave number.

D. Rayleigh-Ritz formula and variational approach

The diagonalization of the transfer matrix and the analytical continuation in $n \to 0$ could in principle be performed exactly due to the rotational invariance of $\mathcal{T}$ in the n-dimensional space of replicated variables. To avoid this tedious calculation, we resort to a Gaussian variational approach whose accuracy and reliability has been recently validated in the case of diffusion on random lattices [25,32].

We start from the Rayleigh-Ritz formula for the largest eigenvalue Λ_0 of a (real-valued) matrix $\mathcal{T}$,

$$\Lambda_0 = \max_{\Psi\neq 0} \mathcal{R}(\Psi) \qquad , \tag{48}$$

where

$$\mathcal{R}(\Psi) = \frac{\langle\Psi|\mathcal{T}|\Psi\rangle}{\langle\Psi|\Psi\rangle} \qquad . \tag{49}$$

A lower bound Λ_0^g to Λ_0 can be obtained through maximization of the r.h.s. of (48) within a suitable trial family of wave functions $\Psi_0^g(Q)$ parametrized by some tunable variables Q. According to (48, 49), we obtain

$$\Lambda_0^g = \mathcal{R}\big(\Psi_0^g(Q_{opt})\big) \qquad , \tag{50}$$

where the optimal parameter Q_{opt} is the solution of

$$\left.\frac{d\mathcal{R}\big(\Psi_0^g(Q)\big)}{dQ}\right|_{Q=Q_{opt}} = 0 \qquad . \tag{51}$$

Notice that within formulation (50,51), $\mathcal{T}$ needs no longer to be real-valued and can assume complex values.

Hereafter, we apply this procedure to the transfer matrix (42) and resort to the following Ansatz,

$$\Psi_0^g(r,\varphi,\vec{x}) = \psi_0(r)\, \exp\left(\frac{i}{4}\, Q(r)\, \vec{x}^2\right) \qquad , \tag{52}$$

where $\psi_0(r)$ is the maximal wave function of the T_0 transfer matrix (9) of Section II.B. This choice ensures that the correct eigenvalue λ_0 is recovered when the number of replicas n strictly equals zero: $\Lambda_0(n) = \lambda_0 + O(n)$. The $\vec{x}$ dependence of the trial wave function (52)results from the similarity of the operator $\mathcal{T}$ (42) with the transfer matrix of a 1D chain of interacting spherical spins, for which the ground state wave function is Gaussian [40]. Furthermore, this Ansatz allows for an exact calculation of the n-dimensional integral over $\vec{x}$ and an easy continuation of the result to real values of n. Note here that the wave function (52) does not depend on φ. This is no assumption for $n = 0$, see Section II.B and supposed to give quantitatively good results for $n > 0$.

The calculation of the Rayleigh-Ritz functional $\mathcal{R}$ (49) with the Gaussian Ansatz (52) is exposed in Appendix A. The resulting functional optimization equation over Q reads

$$\frac{\lambda_0\ \psi_0(r)}{2\ Q(r)} = \int_{r_{min}}^{\infty} dr' \int_0^{\pi} d\theta\ T(r,r',\theta)\ \psi_0(r')\ \frac{Q(r')+\lambda+i\epsilon-d_0(r',r,-\theta)}{\mathcal{W}(r,r',\theta)} \quad , \tag{53}$$

where

$$\mathcal{W}(r,r',\theta) = (Q(r)+\lambda+i\epsilon-d_0(r,r',\theta))(Q(r')+\lambda+i\epsilon-d_0(r',r,-\theta)) - d_1(r,r',\theta)^2 \quad . \tag{54}$$

The solution of the above equation gives access to the variational estimate of the density of modes from (44),

$$\rho^g(\lambda) = -\frac{1}{\pi}\int_{r_{min}}^{\infty} dr\ \psi_0(r)^2\ \mathrm{Im}\left(\frac{1}{Q(r)}\right) \quad . \tag{55}$$

We can pursue the procedure to compute the excited eigenvalues Λ_ℓ of $\mathcal{T}$. Drawing our inspiration from the 1D spherical spins chain transfer matrix [40], we look for a variational wave function of the type

$$\Psi^g_\ell(r,\varphi,\vec{x}) = \Psi^g_0(r,\varphi,\vec{x})\ P^g_\ell(x^1,x^2,\ldots,x^n) \quad , \tag{56}$$

where P^g_ℓ is a polynomial of n variables of total degree ℓ. To obtain the asymptotic behaviour of the resolvent (45), we only need the first excited state $\ell=1$, whose corresponding variational polynomial is clearly $P^g_1(\vec{x}) = x^1$, giving thereby from (49)

$$\begin{aligned}\tau^g = \frac{\Lambda^g_1}{\Lambda^g_0} = -2\left\{\int_{r_{min}}^{\infty} drdr' \int_0^{\pi} d\theta\ T(r,r',\theta)\ \psi_0(r)\ \psi_0(r')\ \frac{d_1(r,r',\theta)}{\mathcal{W}(r,r',\theta)}\right\} \\ \times\left\{\lambda_0\int_{r_{min}}^{\infty} dr\ \psi_0(r)^2 Q(r)^{-1}\right\}^{-1}\end{aligned} \tag{57}$$

in the $n\to 0$ limit as shown in Appendix A.

V. RESULTS AND COMPARISON WITH EXPERIMENTS

A. Numerical resolution of the self-consistent equations

We first compute the ground state wave function $\psi_0(r)$ and the corresponding eigenvalue λ_0, see Section II.B, by means of Kellog's method [27]. The integration range $[r_{min};r_{max}]$ over r is discretized into a set of n_r points r_α, $\alpha=1,\ldots,n_r$ with $r_1 = r_{min} = 9.8\mathring{A}$ and $r_{n_r} = r_{max} = 10.7\mathring{A}$.

Self-consistent equations (53) for $Q(r)$ can then be solved iteratively. As can be checked at zero temperature, convergence is improved by iterating the equations for $1/Q(r)$ rather than for $Q(r)$ itself. We stop the iteration process as soon as the differences between the $1/Q(r_\alpha)$'s and their images through the iteration become smaller than 10^{-7} for all $1\le\alpha\le n_r$.

Numerical difficulties come from the limits $\epsilon\to 0$ and $n_r\to\infty$. This can be best seen for base pairs vibrations in the simplest case $E=0$. The exact solution to equations (53) is $Q(r) = \lambda + i\epsilon - \frac{1}{2}V_m''(r)$. In other words, eigenvalues λ and radii r are in simple correspondance : to any permitted eigenvalue λ is associated one (or a few) radius $r(\lambda)$ such that $\lambda = \frac{1}{2}V_m''(r(\lambda))$ and the density of states reads

$$\rho(\lambda) = \lim_{\epsilon\to 0}\frac{1}{\pi}\int_{r_{min}}^{r_{max}} dr \frac{\psi_0(r)^2\ \epsilon}{(\lambda-\frac{1}{2}V_m''(r))^2+\epsilon^2} = \frac{2}{|V'''(r(\lambda))|}\ \psi_0(r(\lambda))^2 \quad . \tag{58}$$

In practice however, the integral in (58) is discretized as follows

$$\rho(\lambda) = \lim_{\epsilon\to 0}\frac{1}{\pi}\sum_{\alpha=1}^{n_r}\frac{\psi_0(r_\alpha)^2\ \epsilon}{(\lambda-\frac{1}{2}V_m''(r_\alpha))^2+\epsilon^2} \quad . \tag{59}$$

Consider the eigenvalue λ_γ corresponding to radius r_γ for some arbitrary integer γ. Dominant $O(1/\epsilon)$ contributions to the density $\rho(\lambda_\gamma)$ in (59) come from α in the range $\gamma-\Delta\le\alpha\le\gamma+\Delta$ with $\Delta\simeq 2\ n_r\ \epsilon/V'''(r_\gamma)$. Problems arise

when Δ is close to unity. When λ scans the interval $[\lambda_\gamma; \lambda_{\gamma+1}]$, the index of the only (for $\Delta = 1$) contributing term to $\rho(\lambda)$ jumps from $\alpha = \gamma$ to $\alpha = \gamma + 1$ at some intermediate λ which will be a local minimum of the density ρ. Such local fluctuations are pure artifacts of the discretization procedure and must be removed by keeping $\Delta \gg 1$, that is $1/n_r \ll \epsilon \ll 1$. Typical suitable values of the parameters are $\epsilon = 2.10^{-2}$, $n_r = 4.10^3$, giving a spectrum $\rho(\lambda)$ almost normalized to unity (with a small error $\simeq \epsilon$).

Note that the same reasoning holds for the numerical calculation of the torsional spectrum. The discretization of the integral over $0 < \theta < \pi$ must be replaced by a sum involving a large number $n_\theta = 900$ of terms to reach a good accuracy of the results.

B. Radial modes

Radial mode spectra obtained for different choices of D and E are displayed figure 5. They exhibit smooth shapes and Van Hove divergences have been smeared out by thermal disorder, compare to figure 4. As at zero temperature, the overall width of the spectrum is an increasing function of E.

For $E = 4eV/\mathring{A}^2$, the general form of $\rho(\nu)$ is reminiscent of the density of states at zero temperature, with a shoulder in $\nu_- \simeq 75$ cm^{-1} and a maximum in $\nu_+ \simeq 135$ cm^{-1}, in correspondence with the edges of the zero temperature spectrum, $\nu_-^0 = 73.8$ cm^{-1} and $\nu_+^0 = 138.7$ cm^{-1}. A careful analysis even show a quantitative agreement between the density of states at $T = 300$ K and $T = 0$ K for frequencies lying in the range 110 cm$^{-1} < \nu < 130$ cm^{-1}. A similar behaviour, that is the robustness of the central part of the spectrum to (weak) disorder was also observed in [32].

At a weaker stiffness $E = 0.74eV/\mathring{A}^2$, a single bump is observed. The range of allowed frequencies at zero temperatures $\nu_-^0 = 71.5$ cm$^{-1} < \nu < 87.5$ cm^{-1} is indeed too narrow and both peaks merge under the action of thermal disorder. Note that a very small fraction of modes seem to be unstable and give rise to imaginary frequencies, see Section III.B. We however discard them since their integrated sum is smaller than the accuracy ϵ of the calculation.

Figure 6 shows the dispersion relations at ambient temperature for radial modes. The frequency $\nu_r(q)$ is an increasing function of the wave number over the interval $0 \leq q \leq \pi$. Since the range of allowed frequencies is much larger at $T = 300$ K than at $T = 0$ K, there is no general coincidence with the zero temperature dispersion relations as can be seen for $E = 0.74eV/\mathring{A}^2$. For larger stiffness constants, the dispersion relations for both temperatures however coincide for medium wave numbers, *i.e.* when $1 \leq q \leq 2$ roughly. In agreement with the above analysis of the density of states, the effective thermal disorder gets weaker and weaker as the stiffness constant E grows.

When E increases, the molecule becomes more and more rigid since radii r_j less and less fluctuate from base pair to base pair. The wave function $\psi_0(r)$ gets more and more concentrated around the minimum of the Morse potential $r = R$, see figure 2 and the region of integration over r that mostly contributes to the density of states in (55) becomes narrower and narrower. On the opposite, for small E, $\psi_0(r)$ mainly reflects the structure of the Morse well whose flanks are not accessible at zero temperature. The tails of ψ_0 are large and give rise to some tails for the density of states. The cross-over between both regimes takes place at $E \sim D\, a^2$, that is of the order of a few $eV/\mathring{A}^2$.

The inverse coherence length σ_r is plotted figure 7 as a function of frequency. In the central ragion of the spectra, the corresponding autocorrelation lengths are $\xi \simeq 0.7$ for $E = 0.74$ and $\xi \simeq 4$ for $E = 4$ with a more sensitive dependence on ν in the latter case. As expected from the above discussion, ξ increases with E. The values of the coherence length ξ are in good agreement with the equilibrium correlation distance ζ defined through

$$\big\langle (r_j - \langle r \rangle)(r_{j+d} - \langle r \rangle) \big\rangle \propto e^{-d/\zeta} \qquad (d \to \infty) \qquad . \tag{60}$$

A thermodynamical calculation of ζ can be carried out from the knowledge of the excited states of the transfer matrix T_0 confined to the Morse potential [47]. Results are $\zeta \simeq 0.51$ for $E = 0.74$ and $\zeta \simeq 0.93$ for $E = 4$ [47]. Note that ζ is the inverse damping with of the static structure factor whereas $\xi(\nu)$ is an energy (frequency) dependent coherence length.

C. Angular modes

We now turn to the angular spectrum. The density of modes is shown on figure 8. We first concentrate on positive, that is real frequencies. The band edge $\nu_+^0 = 13.6$ cm^{-1} of the zero temperature spectrum visible on figure 4 disappears at finite temperature. A sharp maximum now takes place at $\nu_M \simeq 7$ cm^{-1}. As expected from zero temperature calculations, the width of the peak is smaller than for radial modes and can be estimated to $\Delta\nu \simeq 15$ cm^{-1}.

The densities of states at $E = 0.74$ and $E = 4$ coincide within 0.1%. We have numerically checked that the angular mode spectrum depends extremely weakly on the stiffness constant E over the whole range $0 \leq E \leq \infty$. In other

words, unlike radial modes, angular modes are not sensitive to the width of the ground state wave function ψ_0, *i.e.* to fluctuations of the base pair radius r, see figure 2. This observation is supported by inspection of the variational parameter $Q(r)$ entering wave function (52). At fixed frequency, both imaginary and real parts of $Q(r)$ are indeed almost constant on the whole range of radius $9.8\mathring{A} < r < 10.7\mathring{A}$.

The robustness of the spectrum displayed fig. 8 can be understood by looking at the variations of $d_0(r, r', \theta)$ around the thermal average positions $r = r' = \langle r_n \rangle$ and $\theta = \langle \theta_n \rangle$. The second derivative of d_0 with respect to r at fixed twist angle equals $\partial_r^2 d_0 \simeq 0.045 eV/\mathring{A}^4$ while the range of fluctuations of r is given by the largest squared width of ψ_0 (corresponding to $E = 0$) and reads $\Delta\langle r_n^2 \rangle \simeq 0.04\mathring{A}^2$. Therefore the fluctuations of the radius r modifies d_0 by $\frac{1}{2}\partial_r^2 d_0 . \Delta\langle r_n^2 \rangle \simeq 0.001 eV/\mathring{A}^2$, that is by less than 2% of d_0 typically. Repeating the same calculation for twist-induced fluctuations, we obtain $\partial_\theta^2 d_0 \simeq 20 eV/\mathring{A}^2$ and $\Delta\langle \theta_n^2 \rangle \simeq k_B T/(d_0 R^2) \simeq 0.005\ rad^2$. The resulting variations of d_0 due to changes of twist are of the order of $\frac{1}{2}\partial_\theta^2 d_0 . \Delta\langle \theta_n^2 \rangle \simeq 0.05 eV/\mathring{A}^2$ that is comparable to d_0.

Consequently, an excellent approximation of the angular mode spectrum may be obtained by the following simple argument. Let us call

$$d_0(\theta) = \frac{1}{R^2} \frac{d^2 V_b}{d\theta^2}(R, R, \theta) \tag{61}$$

the diagonal element of $\mathcal{D}^{\mathcal{C}}$ (29) where we have for simplicity identified $\langle r_n \rangle$ with R since $\langle r_n \rangle - R \simeq 0.01\mathring{A} \ll R$ at $T = 300$ K). The twist angle θ is approximately distributed with the Gibbs measure, see (10),

$$p(\theta) = \frac{1}{Y_0(R, R)} \exp\left\{ -\beta V_b\left(R, R, \theta\right)\right\} \quad . \tag{62}$$

Then we may substitute the variational equation (53) on $Q(r)$ with

$$\frac{1}{2\,Q} = \int_0^\pi d\theta\, p(\theta) \frac{Q + \lambda + i\epsilon - d_0(\theta)}{(Q + \lambda + i\epsilon - d_0(\theta))^2 - d_0(\theta)^2} \ , \tag{63}$$

which involves a single parameter Q. Solving equation (63), the density of angular modes equals $-\mathrm{Im}(1/Q)/\pi$ and is in excellent agreement with figure 8. From a numerical point of view, this approximation is much less time consuming than the full resolution of (53). In fact, equation (53) required the integral over θ to be computed for each value of r (and at each iteration step) and the solving time was therefore n_r times larger than for (63).

Close to zero frequency, the density of states vanishes as $\rho_\varphi(\nu) \propto |\nu|$ since the density of eigenvalues $\rho(\lambda)$ is finite in $\lambda = 0$, see (17). We now turn to negative, that is imaginary frequencies. Computing the integrated density of unstable modes, we see that the latters represent roughly 20% of angular modes. They extend down to frequencies equal to $\nu_- = -20$ cm^{-1} with a maximum in $\nu \simeq -3.5$ cm^{-1}. We shall come back to the physical implications of these modes in next Section.

The relation of dispersion $\nu_\varphi(q)$ for the angular modes is displayed figure 9 over the whole range of real and imaginary frequencies. We also show on figure 10 the inverse autocorrelation length $\sigma_\varphi(\nu)$. As for radial modes, the dispersion relations at $T = 300$ K gets close to its zero temperature counterpart at intermediate wave numbers $0.5 \leq q \leq 1.5$ corresponding to frequencies 0 cm$^{-1} \leq \nu \leq 10$ cm^{-1}. This coincidence is accompagnied by small values of σ on this interval of frequencies, giving rise to a coherence length of the order of $\xi \simeq 2$. Conversely, large frequencies correspond to highly disordered modes: $q \geq 2$ and monotonously increasing σ, with $\xi \simeq 0.4$ at $\nu = 30$ cm^{-1}. Notice that the statical correlation length is the same as for radial modes, see Section V.B.

Unstable modes have also short autocorrelation lengths, e.g. $\xi \simeq 0.4$ at $\nu = -20$ cm^{-1}. However, their wave numbers are much smaller and can be considered as contant (and zero) for $\nu \leq -10$. The autocorrelation function of unstable eigenmodes (36) therefore do not change sign over a typical distance $d_s \sim \pi/q \gg 1$. Unstable modes can be seen as unstable acoustic phonons, involving coherent rotations of the molecule extending over regions of size d_s.

To end with, notice that the dispersion relation and the inverse coherence length both exhibit an inflection point in $\nu = 0$ as shown fig. 9 and 10. This is an artefact of the representation of unstable modes as negative frequencies. Consider for instance the damping width σ close to zero frequency. In the natural λ eigenvalue parametrization, we expect a non singular behaviour in the vicinity of $\lambda = 0$: $\sigma(\lambda) = \sigma_0 + \sigma_1 \lambda + O(\lambda^2)$. For positive eigenvalues λ, the frequency ν is defined as $\nu \propto \sqrt{\lambda}$ (17) while using the negative-imaginary convention of Section III.B, $\nu \propto -\sqrt{-\lambda}$ for negative eigenvalues. The expansion of the inverse coherence length as a function of (small) frequencies thus reads: $\sigma(\nu) = \sigma_0 + \tilde{\sigma}_1 \nu . |\nu| + O(|\nu|^3)$ and is singular with an inflection point in $\nu = 0$.

D. Discussion

Our calculation shows that the coherence length of normal modes is finite and remains of the order of unity. Eigenvectors at finite temperature are thus far from being plane waves as in the zero temperature case. The power spectrum, that is the Fourier transform of the autocorrelation function at frequency ν (45) acquires a Lorentzian form centered around a certain wave number $q(\nu)$ with a width $\sigma(\nu)$. This behaviour is experimentally observed in neutron scattering experiments [1,18]. Furthermore, the calculation justifies *a posteriori* the absence of selection rule on momentum in Raman experiments. Indeed, the coherence length of the disordered phonons is of the order of $\xi H \leq 20\mathring{A}$ and is negligible with respect to optical wavelengths $\simeq 4800\mathring{A}$, see Section III.C.

Both radial and angular spectra are superposed in figure 11. The total spectrum $\rho(\nu)$ equals $\rho_r(\nu) + \rho_\varphi(\nu)$ is normalized to unity (half of modes originate from angular degree of freedom, and the remaining half from radial ones). The torsion peak appears much more narrow and higher than its radial counterpart. The width of the latter amounts to $\Delta\nu \simeq 60$ cm^{-1} (respectively $\Delta\nu \simeq 100$ cm^{-1}) for $E = 0.74eV/\mathring{A}^2$ (resp. for $E = 4eV/\mathring{A}^2$) whereas (stable) torsional modes spread over a range of $\Delta\nu \simeq 15$ cm^{-1}. While for $E = 4eV/\mathring{A}^2$, torsional and radial spectra do not intersect each other, there is an overlap region at smaller stiffness constant around $\nu \simeq 30$ cm^{-1}. Nevertheless, both fluctuations take place on basically two distinct scale times. Angular vibrations are associated to a typical frequency of $\simeq 10$ cm^{-1}, or equivalently to a typical time $\tau_v \simeq 3\ 10^{-12}$ s. Radial modes are present at frequencies $\simeq 100$ cm^{-1} that is involve dynamical processes on a scale $\tau_r \simeq 0.3\ 10^{-12}$ s. At low frequencies $|\nu| < 25$ cm^{-1}, the presence of unstable modes threatens the validity of the linearization procedure used in Section III.B. A more refined analysis taking into account non linear terms in the dynamical equations is needed to understand how unstable modes (with low wave numbers q) are coupled to stable mode (with larger q) and modify the frequencies of the latters. the influence of viscous friction upon modes in this frequency regime would also deserve to be further studied as mentioned Section III.A. Conversely, the absence of unstable modes at frequencies larger than $\nu > 25$ cm^{-1} indicate that the INM predictions are reliable for time scale smaller than 10^{-12} s. This is enough to identify the range of allowed frequencies for torsional modes: $\nu < 30$ cm^{-1}. The INM prediction for the location of the torsional peak $\nu_M \simeq 7$ cm^{-1} cannot be trust blindly but it reasonably lies in the middle of the zero temperature band, see Section III.D.

We now turn to the comparison with spectroscopy measurements. To establish the link between the density of states and the Raman intensity, the knowledge of the light-to-vibrations coupling $C(\nu)$ is necessary as seen Section III.C. In the absence of precise information on the latter, we have rescaled the density of modes $\rho(\nu)$ according to formula (18) for the three different choices $C(\nu) = 1$, $C(\nu) = \nu$ and $C(\nu) = \nu^2$ (note that the second hypothesis for C is the most plausible one). The resulting theoretical Raman intensities are shown figure 12.a for $E = 0.74eV/\mathring{A}^2$ and figure 12.b for $E = 4eV/\mathring{A}^2$. From the one hand, the overall shape of the spectra change with C with respect to ρ. In particular for $C(\nu) = 1$ and $C(\nu) = \nu$, the torsional peak diverges at small frequencies and the radial modes bump acquires a shoulder from, located in the right flank of the torsional modes. On the other hand, the band of allowed frequencies remains unaltered by the choice of C and extends over $50 < \nu < 110$ cm^{-1} for $E = 0.74$ and $50 < \nu < 150$ cm^{-1} for $E = 4$. In the latter case, the radial region of the spectrum exhibit two local maxima at the same height for $C(\nu) = \nu$. The rescaled spectrum of fig 12.a for $C(\nu) = \nu$ closely agrees with intensity curves obtained from Raman experiments at $T = 50^o$C and shown figure 2 of Ref. [5] on the range of frequencies $50 < \nu < 110$ cm^{-1}. The latter measurement was performed on calf thymus in solution (10 mM PHB, ph=7). This allows us to think that $E = 0.74$ is a better choice for the stiffness constant than $E = 4$ [27].

Our results do not show drastic variations with temperature for T ranging from 300 K to the melting temperature $T_m = 350$ K. At T_m the double helix structure disappears and so do all angular and radial vibrations. Since denaturation is described as a first order phase transition by the present model, there is no gradual destabilization of the modes and no relevant change in ρ can be seen as mentioned above. The experimental Raman measurements shown on figure 2 of Ref. [5] nevertheless show a smooth change in the shape of the intensity curves over the temperature interval 50^oC$< T < 80^o$C. This apparent paradox can be easily explained by the fact that our model describes a homogeneous sequence of bases. For the latter, the fraction of open base pairs versus temperature exhibits an abrupt jump from zero to one at T_m [39]. In the case of a heterogeneous sequence as in the experiments of Ref. [5], the denaturation temperature of AT rich regions can be inferred to be $T_m = 50^o$C [39] and the fraction of open base pairs smoothly increases from zero to one over the range of temperatures 50^oC$< T < 77^o$C.

We now turn to angular modes. Raman measurements on fibers at 100% of relative humidity (r.h.) have given evidence for a narrow band at 16cm^{-1}, see fig. 1 of Ref. [7]. This peak shifts down to lower frequencies (10cm^{-1}) when increasing the hydration degree of DNA in gels and disappears in the central component for DNA in solution [5]. Other measurements on B-DNA fibers al lower $\simeq 80\%$ r.h. by Lindsay et al. have reported a similar band at a higher frequency $\nu \simeq 25$cm^{-1} that shifts to lower values as the r.h. increases in good agreement with Urabe et al.'s data [8]. The observed softening of the frequence may come from the weakening of external e.g. interhelical interactions as

well as from the influence of the (rigid) primary and (viscous) secondary water shells, see Section III.A. Note that this modes seems to appear when the scattering vector $\Delta\vec{Q}$ gets parallel to the helical axis. Other molecular system as crystals of ATP or guanosine monosphosphate (GMP) that present a columnar stacking of bases (even without hydrogen bond interactions) exhibit similar low frequency spectra. The intensity of the low frequency ($< 20\text{cm}^{-1}$) mode was found to depend mostly on the stacking degree of bases in a column [9]. Our calculation predicts, despite the presence of unstable INM and the absence of friction terms in the dynamical equations (11) that angular modes are predominant for $\nu < 25\text{cm}^{-1}$. At such low frequencies, radial modes can be neglected and twist fluctuations are responsible for collective vibrations of interplane distances h_n. In agreement with experiments, our calculation thus predicts that low frequency modes ($\nu < 25\text{cm}^{-1}$) are related to vibrations of the base pairs column.

A quantitative comparison of our dispersion relations for angular modes with experimental results is difficult to the lack of available data. Neutron scattering measurements have shown that pseudo-dispersion relations with a finite damping width can be obtained for low frequencies but these experiments have been performed on crystalline DNA fibers. Our model (and the values of parameters exposed Section II.C) are valid for DNA in solution where the interaction with surrounding water is radically different and interhelical effects are absent. More precisely, we find that at fixed momentum q, the experimental frequency ν for fibers is larger than the theoretical predictions for diluted DNA. The additional mass due to primary water shells for DNA in solution may account for the reduction of frequency to a large extent [8]. Conversely, the extrapolated value of σ is constant and equal to 0.48 in good agreement with the theoretical minimum $\sigma = 0.5$ shown fig. 10.

VI. SUMMARY AND CONCLUSION

In this article, we have shown how to apply the INM framework to a simple model of DNA molecule and reproduce the main features of collective vibration modes at finite temperature. Scale time separation between atomic vibrations and collective modes allows to obtain good results at low frequencies without resorting to a detailed description of DNA at the atomic level. This simplified modelization of DNA permits in turn a deeper analytical understanding of the structure of the modes than e.g. within MSPA.

The model we had introduced to reproduce thermally and mechanically-induced DNA denaturation transitions has proven to be also capable of describing accurately the pico-second dynamics seen through spectroscopy measurements. This robustness has been obtained without any modification of the model or any new fit of the constant force or geometrical parameters. Remarkably, the comparison with Raman experiments has permitted us to decide the value of the only parameter known with some uncertainty from the denaturation experiments, that is the stacking stiffness E. The success of the present model to account for completely different experiments comes from its mesoscopic nature, that lies at an intermediate level between microscopic modelizations, e.g. studies by Prohofsky *et al.* [10] or numerical simulations by Lavery and collaborators [48] and elasticity theories as the Worm-Like-Chain model [49] and its recent extensions [50].

Our calculation gives access to the density of modes $\rho(\nu)$ and some statistical properties of the normal modes as the dispersion relation $\nu(q)$ and the autocorrelation length $1/\sigma(\nu)$. The dispersion relations provide the power spectrum of the modes which exhibit a finite damping width σ at ambient temperature.

Let us summarize briefly our main quantitative result. Through a rescaling of the density of modes taking into account the light-to-vibrations coupling C, we have related the density of modes to Raman intensity measurements. The choice of parameters $D = 0.15eV$, $E = 0.74eV/\mathring{A}^2$ offers a good agreement with the experiments by Urabe et al. (see figure 12.a and figure 2 in [5]). The range of frequencies 50 $\text{cm}^{-1} < \nu < 100$ cm^{-1} corresponding to radial, *i.e.* base pair stretching modes do not qualitatively depend on C. Furthermore, it remains roughly unchanged in the whole interval of temperatures $0^o\text{C} < T < T_m$ where $T_m = 77^o\text{C}$ is the denaturation temperature. Indeed, our model describes a homogeneous sequence for which the melting transition is very abrupt and not smooth as for disordered DNA.

It would be very interesting to compare our theoretical results for $\sigma_r(\nu)$ and $\nu_r(q)$ with neutron scattering experiments which to our best knowledge are not available for DNA in solution over the range of frequencies mentioned above. A fundamental feature of the modes is that the coherence length ξ is of the order of unity: decorrelation between components of the same mode takes place on a few Angströms. This prediction agrees well with results for the static correlation distance ζ obtained from statistical mechanics calculations as seen Section V.B.

As for angular modes, the predicted characteristic frequencies $\nu < 25$ cm^{-1} coincide with the Raman measurements $\nu < 16$ cm^{-1} [9]. The value of the coherence length in the center of the spectrum, $\xi = 1/\sigma \simeq 6.8\mathring{A}$ is compatible with data obtained through neutron scattering experiments on DNA fibers [1]. However, as far as angular modes are concerned, the present approach suffers from two weaknesses . First, we have not taken into account in the dynamical equations the viscous forces that might become relevant at very low frequencies. Secondly, INM can become unstable

at small ν and the linearization approximation we have used throughout the study reveals dangerous. Further information about the non linear couplings between modes would be extremely useful to circumvent this difficulty. It is however not clear how such a study could be technically pursued.

Acknowledgments : We are particularly grateful to W. Baumruk and P.Y. Turpin for motivating and enligthening discussions on the experimental aspects of this work. We also thank J.F. Leger, L. Bourdieu, A. Colosimo, D. Chatenay, M. Peyrard and H. Urabe for advises and discussions.

APPENDIX A: VARIATIONAL CALCULATION AND SELF-CONSISTENT EQUATION FOR Q

In this Appendix, we compute the Rayleigh-Ritz functional for both the ground state (52) and the first excited (56) (with $\ell = 1$) wave functions. We then derive the saddle-points equations on the variance $Q(r)$ for both instantaneous modes families.

1. Calculation of the ground state

Inserting the Gaussian Ansatz (52) in (49), we obtain

$$\begin{aligned}\mathcal{R}[\Psi_0^g] &= \frac{\int_{r_{min}}^{\infty} dr dr' \int_0^{\pi} d\theta\; T(r,r',\theta)\; \psi_0(r)\; \psi_0(r')\; \left\{\mathcal{W}(r,r',\theta)\right\}^{-n/2}}{\int_{r_{min}}^{\infty} dr\; \psi_0(r)^2\; \left\{ -8\pi\; i\; Q(r)\right\}^{-n/2}} \\ &= \lambda_0 + \frac{n}{2}\; r^g[Q] + O(n^2) \end{aligned} \tag{A1}$$

where $\mathcal{W}$ (54) is the determinant of the two by two matrix $\mathcal{M}$ defined by

$$\mathcal{M} = \begin{pmatrix} Q(r) + \lambda + i\epsilon - d_0(r,r',\theta) & d_1(r,r',\theta) \\ d_1(r,r',\theta) & Q(r') + \lambda + i\epsilon - d_0(r',r,-\theta) \end{pmatrix} \quad , \tag{A2}$$

and

$$\begin{aligned} r^g[Q] = \lambda_0 & \int_{r_{min}}^{\infty} dr\; \psi_0(r)^2 \ln Q(r) \\ & - \int_{r_{min}}^{\infty} dr dr' \int_0^{\pi} d\theta\; T(r,r',\theta)\; \psi_0(r)\; \psi_0(r')\; \ln \mathcal{W}(r,r',\theta) \end{aligned} \tag{A3}$$

up to an irrelevant additional constant. The vanishing condition (51) on the functional derivative of $r^g[Q]$ with respect to $Q(r)$ leads to equation (53).

2. Calculation of the first excited state

We now compute Λ_1^g using Ansatz (56) and expression (49). The denominator of $\mathcal{R}[\Psi_1^g]$ reads

$$\begin{aligned}\langle \Psi_1^g | \Psi_1^g \rangle &= \int_{r_{min}}^{\infty} dr \int_{-\infty}^{\infty} d\varphi \int d\vec{x}\; \psi_0(r)^2\; x_1^2\; \exp\left(\frac{i}{2} Q(r)\; \vec{x}^2\right) \\ &= i\; C\; \int_{r_{min}}^{\infty} dr\; \psi_0(r)^2\; Q(r)^{-1} \quad , \end{aligned} \tag{A4}$$

when $n \to 0$. $C = \int_{-\infty}^{\infty} d\varphi$ could be made finite by limiting the range of the twist angle. Such a regularization is however not necessary since C also appears in the numerator of (49),

$$\langle \Psi_1^g | \mathcal{T} | \Psi_1^g \rangle = \int_{r_{min}}^{\infty} dr dr' \int_{-\infty}^{\infty} d\varphi d\varphi' \; T(r, r', \varphi - \varphi') \; \psi_0(r) \; \psi_0(r') \; \times$$
$$\times \int d\vec{x} d\vec{x}' \; x_1 x_1' \; \exp\left[\frac{i}{4} \begin{pmatrix} \vec{x} \\ \vec{x}' \end{pmatrix}^{\dagger} . \mathcal{M} . \begin{pmatrix} \vec{x} \\ \vec{x}' \end{pmatrix} \right]$$
$$= 2\, i\, C \int_{r_{min}}^{\infty} dr dr' \int_0^{\pi} d\theta \; T(r, r', \theta) \; \psi_0(r) \; \psi_0(r') \left(\mathcal{M}^{-1} \right)_{12} (r, r', \theta) \qquad , \tag{A5}$$

as the number of replicas n vanishes. Using $\Lambda_0^g \to \lambda_0$ when $n \to 0$, we obtain equation (57).

3. Case of base pairs vibrations

For base pair vibrations, the second derivatives d_0 and d_1 are given in (30) and do not depend on the relative twist θ between successive base pairs. Inserting (30) into the extremization equation (53) for $Q(r)$ and using the definition (9) of the effective radial transfer matrix T_0, we obtain

$$\frac{\lambda_0 \; \psi_0(r)}{2 \; Q(r)} = \int_{r_{min}}^{\infty} dr' \; T_0(r, r') \; \psi_0(r') \; \frac{Q(r') + \lambda + i\epsilon - \frac{1}{2} V_m''(r') - 2E}{\mathcal{W}_r(r, r')} \qquad , \tag{A6}$$

where

$$\mathcal{W}_r(r, r') = \left(Q(r) + \lambda + i\epsilon - \frac{1}{2} V_m''(r) - 2E \right) \left(Q(r') + \lambda + i\epsilon - \frac{1}{2} V_m''(r') - 2E \right) - 4E^2 \; . \tag{A7}$$

The ratio (57) of the first two eigenvalues of $\mathcal{T}$ is given by

$$\frac{\Lambda_1^g}{\Lambda_0^g} = -4E \left\{ \int_{r_{min}}^{\infty} dr dr' \; \frac{T_0(r, r')}{\mathcal{W}_r(r, r')} \; \psi_0(r) \; \psi_0(r') \right\} \Big/ \left\{ \lambda_0 \int_{r_{min}}^{\infty} dr \; \psi_0(r)^2 Q(r)^{-1} \right\} \qquad . \tag{A8}$$

4. Case of twist angle fluctuations

For twist fluctuations, the elements d_0, d_1 of the matrix $\mathcal{D}_{\varphi}^{\mathcal{C}}$ of second derivatives depend on radii r, r' as well as on the angle θ. No simplification arises as in the base pairs case. The saddle-point equation for $Q(r)$ is precisely equation (53) but care must be paid to the backbone potential $V_b(r, r', \theta)$. As can be seen from definition (4), the angular integral in (53) is restricted to twist angles θ fulfilling the condition

$$\cos\theta > \frac{r^2 + r'^2 - L^2}{2 \; r \; r'} \qquad . \tag{A9}$$

Indeed, when the inequality in (A9) is not satisfied, the potential V_b is infinite, see discussion of Section II.A. The same prescription holds for the angular integral in (57).

---

* Email: cocco@lpt.ens.fr, monasson@lpt.ens.fr
preprint 99/40; LPTENS is a unité mixte du CNRS, associée à l'Ecole Normale Supérieure et à l'Université de Paris–Sud.

[1] H. Grimm, H. Stiller, C.F. Majkrazak, A. Rupprecht, U. Dahlborg, *Phys. Rev. Lett.* **59**, 1780 (1987).
[2] H. Grimm, A. Rupprecht, *Physica B* **174**, 291 (1991).
[3] H. Grimm, A.Rupprecht, *Physica B* **234-236**, 183 (1997).
[4] P. Painter, L. Mosher, C. Rhoads, *Biopolymers* **20**, 243 (1981).
[5] H. Urabe, Y.Tominaga, *J. Phys. Soc. of Japan* **50**, 3543 (1981).
[6] H. Urabe, Y.Tominaga, K. Kubota, *J. Chem. Phys.* **78**, 3543 (1983).
[7] H. Urabe, H. Hayashi, Y. Tominaga, Y. Nishimura, K. Kubota, M. Tsuboi, *J. Chem. Phys.* **82**, 531 (1985).

[8] S.M. Lindsay, S.A. Lee, J.W. Powell,T. Weidlich, C. Demarco, G.D. Lewen, N.J. Tao, A. Rupprecht, Biopolymers **27** 1015 (1988).
[9] H. Urabe, Y. Sugawara, M. Tsukakoshi, T. Kasuya, *J. Chem. Phys.* **95**, 5519 (1991).
[10] E.W. Prohofsky, *Statistical Mechanics and Stability of Macromolecules*, Cambridge University Press, Cambridge (1995).
[11] J.M. Eyster, E.W. Prohofsky, *Biopolymers* **13**, 2505 (1974); 2527 (1974).
[12] Y. Gao, K.V. Devi-Prasad, E.W. Prohofsky, *J. Chem. Phys.* **80**, 6291 (1984).
[13] Y.Z. Chen, E.W. Prohofsky, *Phys. Rev. E* **49**, 873 (1993).
[14] Y.Z. Chen, E.W. Prohofsky, *Phys. Rev. E* **49**, 3444 (1993).
[15] Y.Z. Chen, Y. Zhang, E.W. Prohofsky, *Phys. Rev. E* **55**, 5843 (1997).
[16] V. Lisy, P. Miskovsky, P. Schreiber, *J. Biomol. Struct. Dyn.* **13**, 707 (1996).
[17] C. Kittel, *Introduction to Solid State Physics*, John Wiley, New-York (1986).
[18] V.V Prabhu, W.K. Schroll, L.L. Van Zandt, E.W. Prohofsky, *Phys. Rev. Lett.* **60**, 1587(1988); H. Grimm, H. Stiller, *Phys. Rev. Lett.* **60**, 1588 (1988).
[19] R. Shuker, R. Gammon *Phys. Rev. Lett.* **25**, 222 (1970).
[20] A.J. Martin, W. Brenig, *Phys. Status Solidi B* **64**, 163 (1974).
[21] B. Souillard, *"Waves and electrons in random media"*, Chance and Matter, Les Houches session XLVI, Elsevier Science (1986).
[22] S.R. Elliott, *Physics of Amorphous Materials*, Longman Scientific and Technical, London (1990).
[23] T. Keyes, *J. Phys. Chem.* A **101**, 2921 (1997).
[24] Y. Wan, R. Stratt, *J. Chem. Phys.* **100**, 5123 (1994).
[25] G. Biroli and R. Monasson, *J. Phys. A* **32**, L255 (1999)
[26] A. Cavagna, I. Giardina, G. Parisi, *Phys. Rev. Lett.***83**, 108 (1999).
[27] S. Cocco, R. Monasson, *Statistical Mechanics of Torque Induced Denaturation of DNA*, cond-mat 9904277; to appear in *Phys. Rev. Lett.* (1999).
[28] S.B. Smith, L. Finzi, C. Bustamante, Science **258**, 1122 (1992).
[29] R.H. Austin, J.P. Brody, E.C. Cox, T. Duke, W. Volkmuth, *Physics Today*, 32 (Feb. 1997) and references therein.
[30] T.R. Strick, J.-F. Allemand, D. Bensimon, A. Bensimon, V. Croquette, *Science* **271**, 1835 (1996).
[31] T.R. Strick, J.-F. Allemand, D.Bensimon, R. Lavery, V. Croquette, *Physica A* **263**, 392-404 (1999).
[32] R. Monasson, *Diffusion, localization and dispersion relations on "small-world" lattices*, cond-mat 9903347; to appear in *EPJ B* (1999).
[33] D.J. Thouless, *Physics Reports* **13**, 93 (1974); Mesoscopic quantum physics, Les Houches session LXI, (Elsevier Science, 1995)
[34] M. Barbi, S. Cocco, M. Peyrard, *Phys. Lett. A* **253**, 358-369 (1999).
[35] M. Peyrard, A.R. Bishop, *Phys. Rev. Lett.* **62**, 2755 (1989).
[36] T. Dauxois, M. Peyrard, *Phys. Rev. E* **51**, 4027-4040 (1995).
[37] J. A. McCammon, S.C. Harvery, *Dynamic of proteins and nucleic acids* , Cambridge University Press (1987).
[38] Y. Zang, W. Zheng, J. Liu, Y.Z. Chen, *Phys. Rev. E* **56**, 7100-7115 (1997).
[39] W. Saenger, *Principles of Nucleic Acid Structure*, Springer-Verlag, New-York (1984);
C.R. Calladine, H.R. Drew, *Understanding DNA*, Academic Press, San Diego (1997).
[40] G. Parisi, *Statistical Field Theory*, Addison-Wesley Publishing, Redwood City CA (1988).
[41] H. Urabe, Y. Sugawara, M. Ataka, A. Rupprecht, *Biophys. J.* **74**, 1533 (1998).
[42] S. N. Volkov, A.M. Kosevich, *J. Biomol. Struct. Dyn.* **8**, 1069 (1991).
[43] Y. Tominaga, K. Kubota, H. Urabe, Y. Nishimura, M. Tsuboi, *J. Chem. Phys.* **83**, 5972 (1985).
[44] V.K. Malinovsky, V.N. Novikov, P.P. Parshin, A.P. Sokolov, M.G. Zemlyanov, *Europhys. Lett.* **11**, 43 (1990).
[45] A. P. Sokolov, A. Kisliuk, D.Quitmann, E. Duval, *Phys. Rev. B* **48**, 7692 (1993).
[46] J.M. Luck, *Systèmes désordonnés unidimensionels*, Aléa Saclay, (1992)
[47] S. Cocco, R. Monasson, *in preparation.*
[48] A. Leburn, R. Lavery, *J. Biomol. Struct. Dyn.* **16**, 593 (1998).
[49] J.F. Marko, E. Siggia, *Science* **265**, 506 (1994).
[50] C. Bouchiat, M. Mézard, *Phys. Rev. Lett.* **80**, 1556 (1997).

TABLES

D (eV)	E $(eV/\mathring{A}^2)$	ΔG (k_BT)
0.15	0.74	0.762
0.16	4	0.825
0.17	12	0.691

Table 1: Three choices of the depths of the Morse potential D and of the stacking stiffnesses E giving the desired melting temperature $T_m = 350$ K. The corresponding denaturation free-energies ΔG are expressed in unit of k_BT at $T = 300$ K.

FIGURE CAPTIONS

Figure 1: The helicoidal DNA model: each base pair is modelized through its radius r_j and angle φ_j. The axial distance h_j between successive base pairs planes varies while the backbone length along the strands is fixed to L.

Figure 2: Ground state wave functions $\psi_0(r)$ at $T = 27^o$C for two choices of the energetic parameters: $D = 0.15eV$, $E = 0.74eV/\mathring{A}^2$ (full curve) and $D = 0.16eV$, $E = 4eV/\mathring{A}^2$ (dotted curve).

Figure 3: Dispersion relations at zero temperature. From bottom to top: $\nu_\varphi(q)$ for torsion modes, $\nu_r(q)$ for radial modes with two different choices of the parameters $D = 0.15eV$, $E = 0.74eV/\mathring{A}^2$ (full curve) and $D = 0.16eV$, $E = 4eV/\mathring{A}^2$ (dotted curve).

Figure 4: Density of states at zero temperature. From left to right: torsion modes spectrum $\rho_\varphi(\nu)$, radial modes spectra $\rho_r(\nu)$ for $D = 0.15eV$, $E = 0.74eV/\mathring{A}^2$ (full curve) and $D = 0.16eV$, $E = 4eV/\mathring{A}^2$ (dotted curve).

Figure 5: Spectra $\rho_r(\nu)$ for radial modes at temperature $T = 27^o$C. Parameters are: $D = 0.15eV$, $E = 0.74eV/\mathring{A}^2$ (full curve) and $D = 0.16eV$, $E = 4eV/\mathring{A}^2$ (dotted curve). Each spectrum is normalized to one half. Note the small oscillations on the tails of the curves due to numerical artifacts, see Section V.A.

Figure 6: Dispersion relations $\nu_r(q)$ for radial modes at temperature $T = 27^o$C. Parameters are: $D = 0.15eV$, $E = 0.74eV/\mathring{A}^2$ (full curve) and $D = 0.16eV$, $E = 4eV/\mathring{A}^2$ (dotted curve). For comparison, dispersion relations at zero temperature are recalled ($E = 0.74eV/\mathring{A}^2$: dashed curve, $E = 4eV/\mathring{A}^2$: dash-dotted curve).

Figure 7: Inverse coherence length $\sigma_r(\nu)$ for radial modes at temperature $T = 27^o$C. Parameters are: $D = 0.15eV$, $E = 0.74eV/\mathring{A}^2$ (full curve) and $D = 0.16eV$, $E = 4eV/\mathring{A}^2$ (dotted curve).

Figure 8: Spectra $\rho_\varphi(\nu)$ for angular modes for $D = 0.16eV$, $E = 4eV/\mathring{A}^2$. The curve for $D = 0.15eV$, $E = 0.74eV/\mathring{A}^2$ is indistinguishable from the latter and from the approximation (61,62,63). The spectrum is normalized to one half. Negative frequencies represent unstable modes according to the convention exposed in Section III.B.

Figure 9: Dispersion relation $\nu_\varphi(q)$ for angular modes (full curve). For comparison, the dispersion relation at zero temperature is recalled (dashed curve). Negative frequencies represent unstable modes according to the convention exposed in Section III.B. Note the inflection point at $\nu = 0$ due to this representation, see Section V.C.

Figure 10: Inverse coherence length $\sigma_\varphi(\nu)$ for angular modes. Negative frequencies represent unstable modes according to the convention exposed in Section III.B. Note the inflection point at $\nu = 0$ due to this representation, see Section V.C.

Figure 11: Spectrum $\rho(\nu)$ for both radial and angular modes Parameters are: $D = 0.15eV$, $E = 0.74eV/\mathring{A}^2$ (full curve) and $D = 0.16eV$, $E = 4eV\mathring{A}^2$ (dotted curve). Each spectrum is normalized to unity

Figure 12: Rescaled spectra for different light-to-vibrations coupling C for parameters $D = 0.15eV$, $E = 0.74eV/\mathring{A}^2$ (**a**) and $D = 0.16eV$, $E = 4eV/\mathring{A}^2$ (**b**). Original spectra $\rho(\nu)$ are recalled (full lines) and rescaling functions are: $C(\nu) = 1$ (dotted curve), $C(\nu) = \nu$ (dashed curve) and $C(\nu) = \nu^2$ (dashed-dotted curve). Vertical units are arbitrary, all curves have been multiplied by a constant to meet (and equal unity) in $\nu = 50$ cm^{-1}.

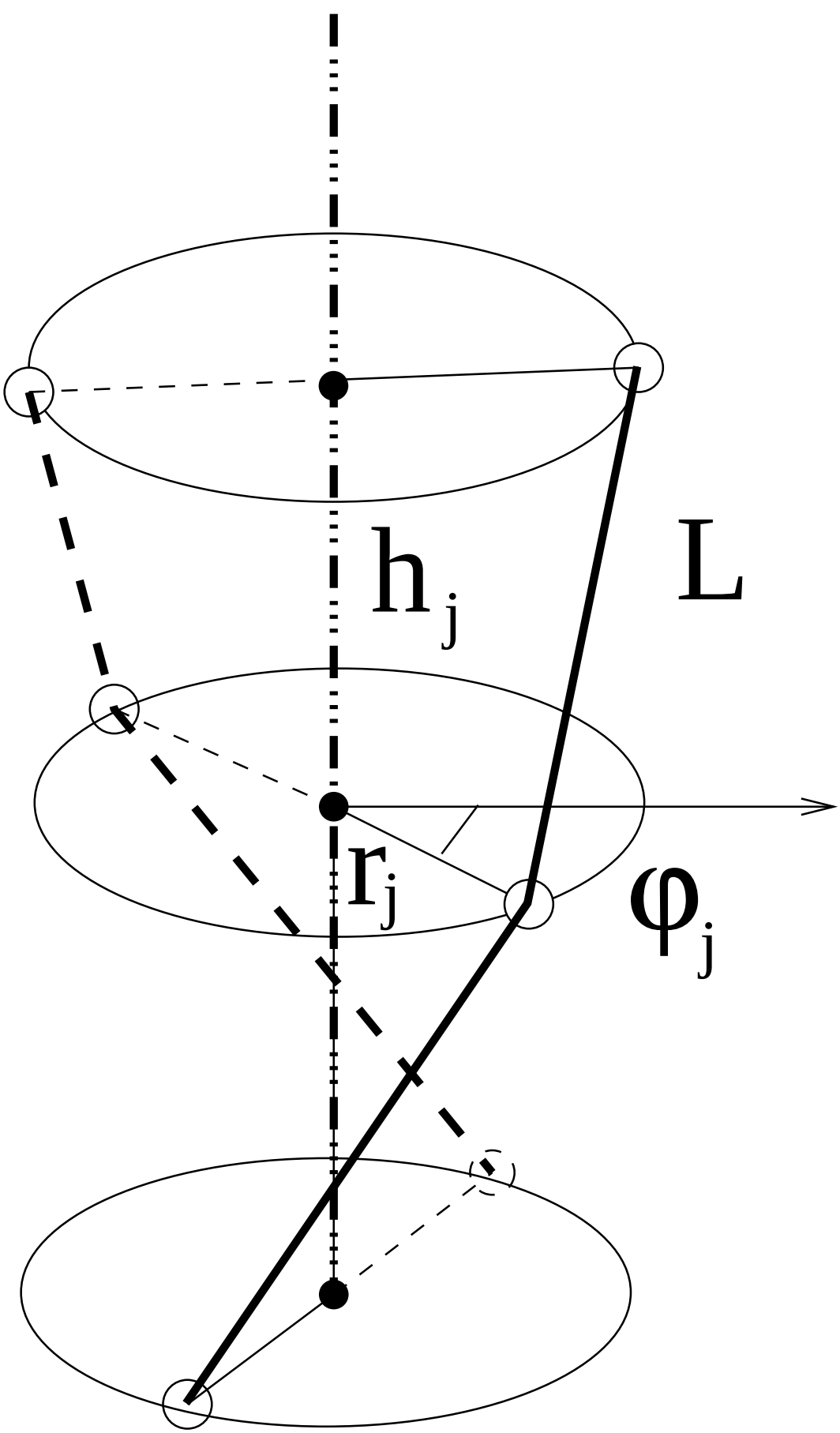
h j
L
r j
φ j

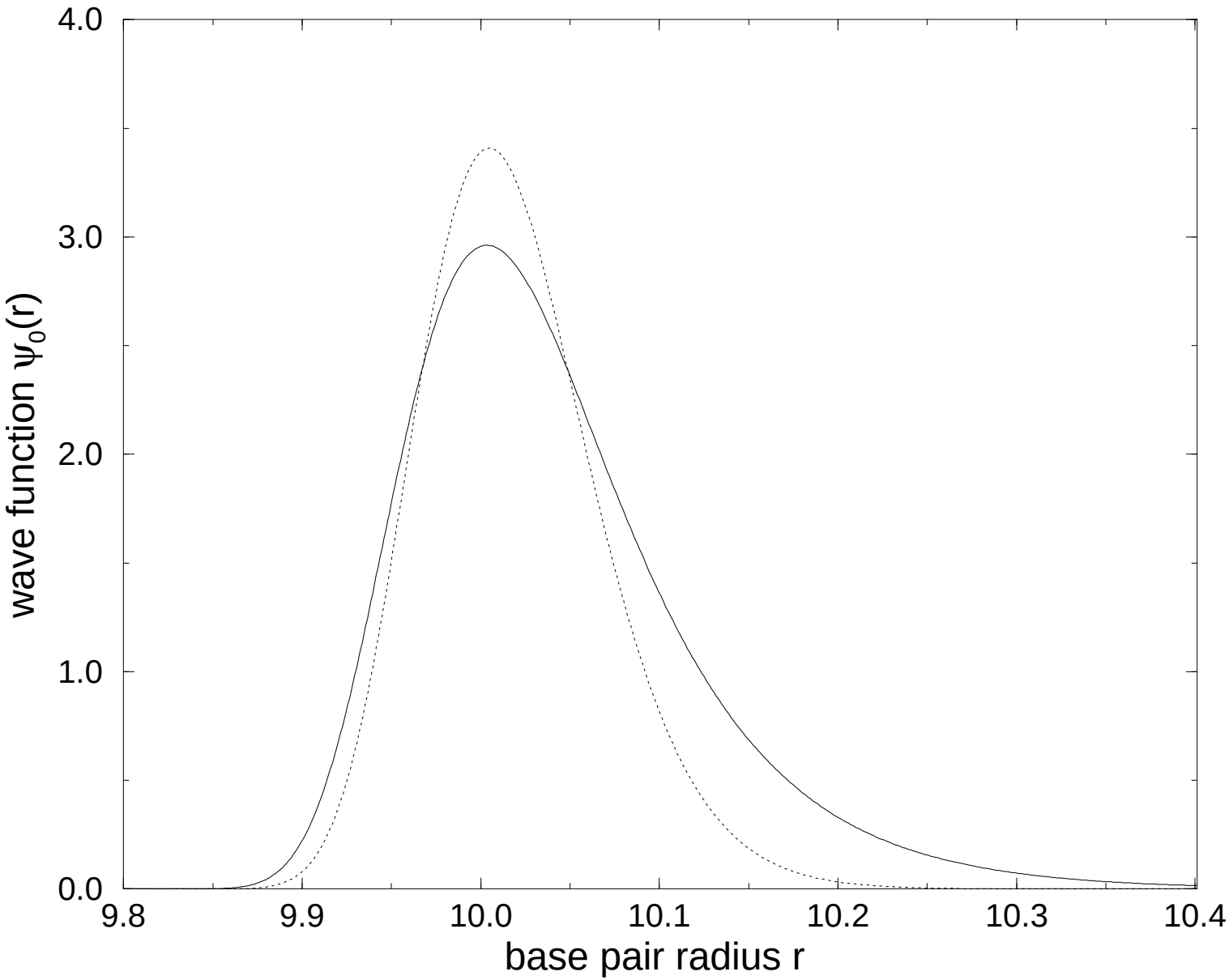
4.0
3.0
2.0
1.0
0.0
wave function $\psi_0(r)$
9.8
9.9
10.0
10.1
10.2
10.3
10.4
base pair radius r

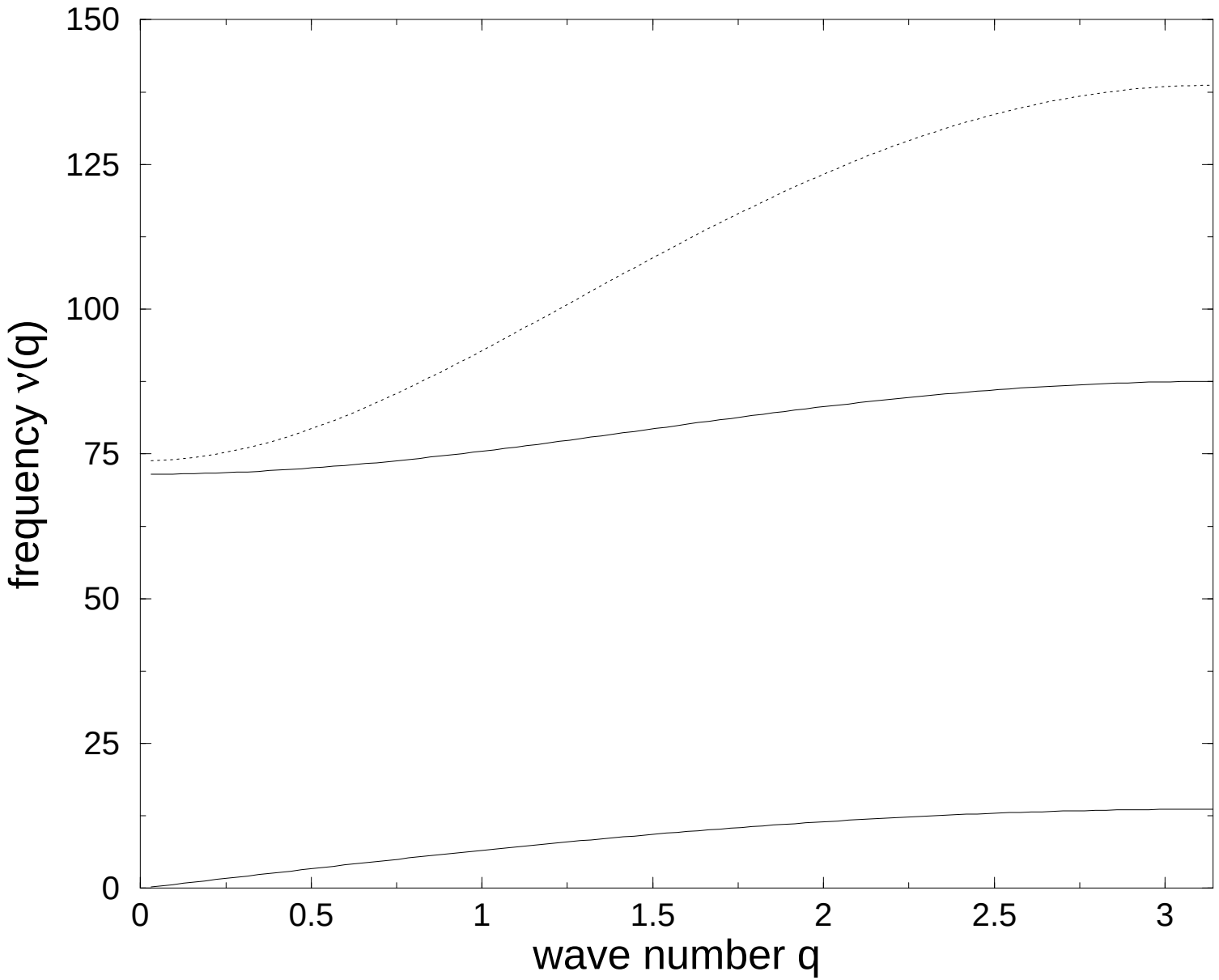
150
125
100
75
50
25
0
0
0.5
1
1.5
2
2.5
3
frequency ν(q)
wave number q

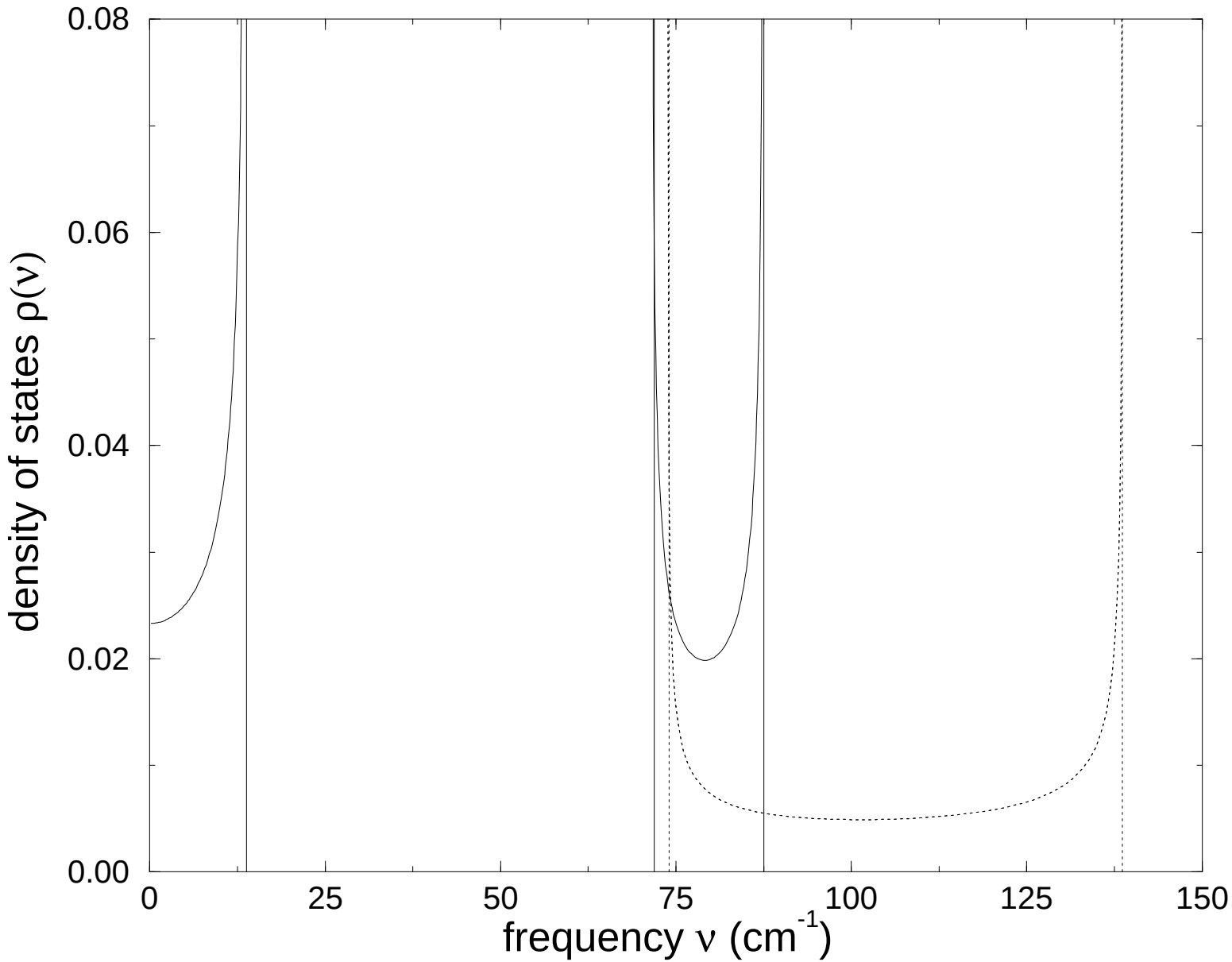
0.08
0.06
0.04
0.02
0.00
density of states ρ(ν)
0
25
50
75
100
125
150
frequency ν (cm-1)

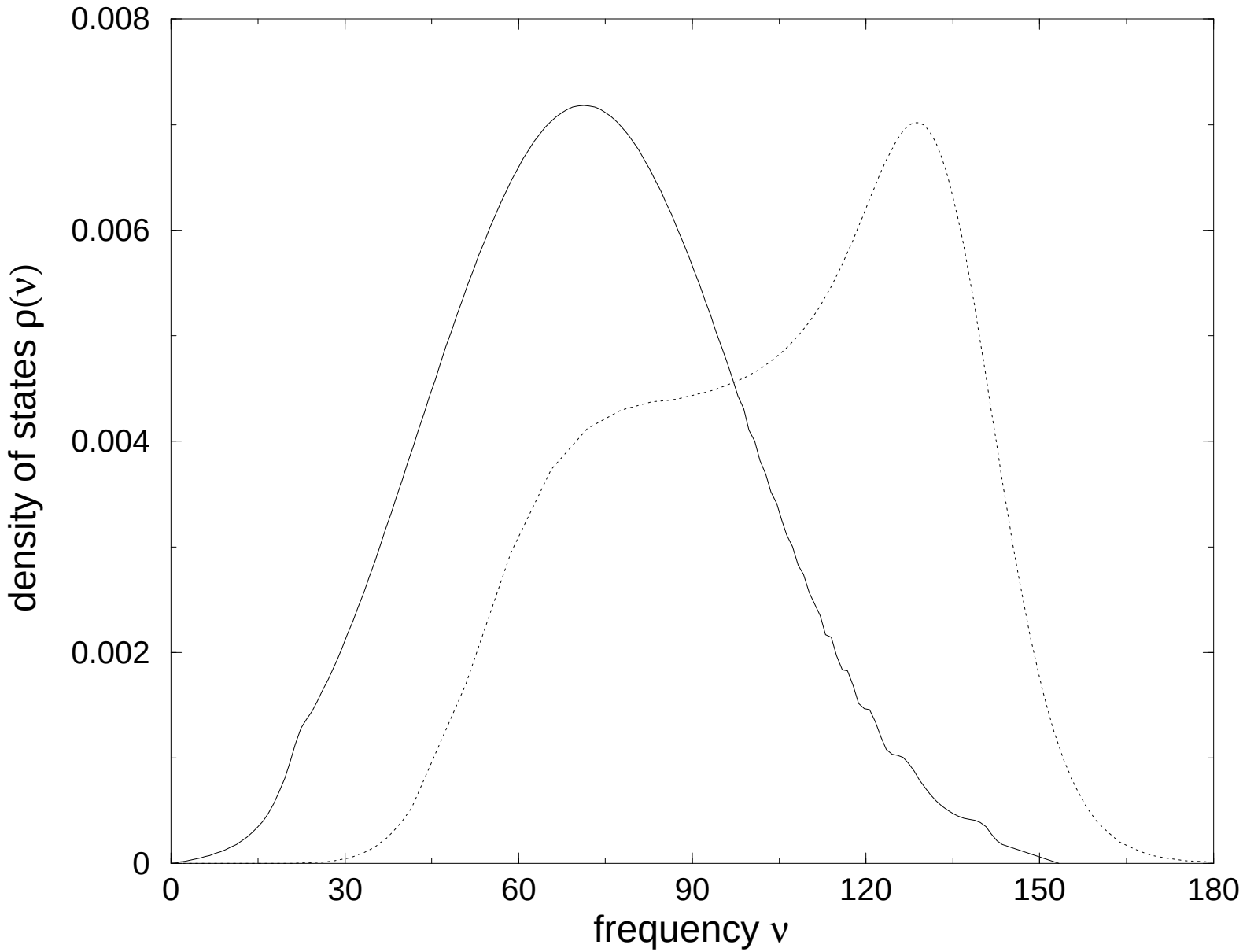
0.008
0.006
0.004
0.002
0
density of states ρ(ν)
0
30
60
90
120
150
180
frequency ν

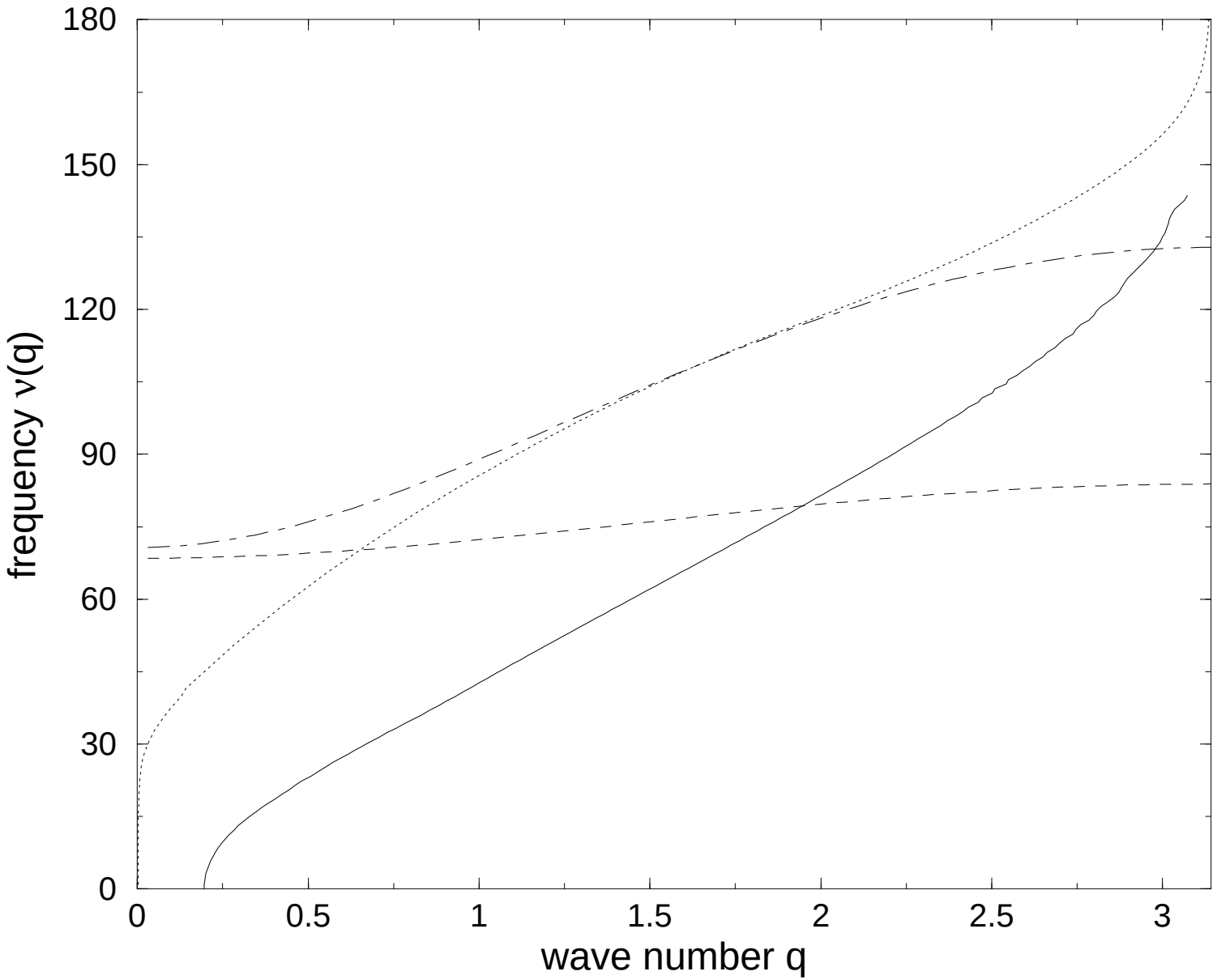
180
150
120
90
60
30
0
frequency ν(q)
0
0.5
1
1.5
2
2.5
3
wave number q

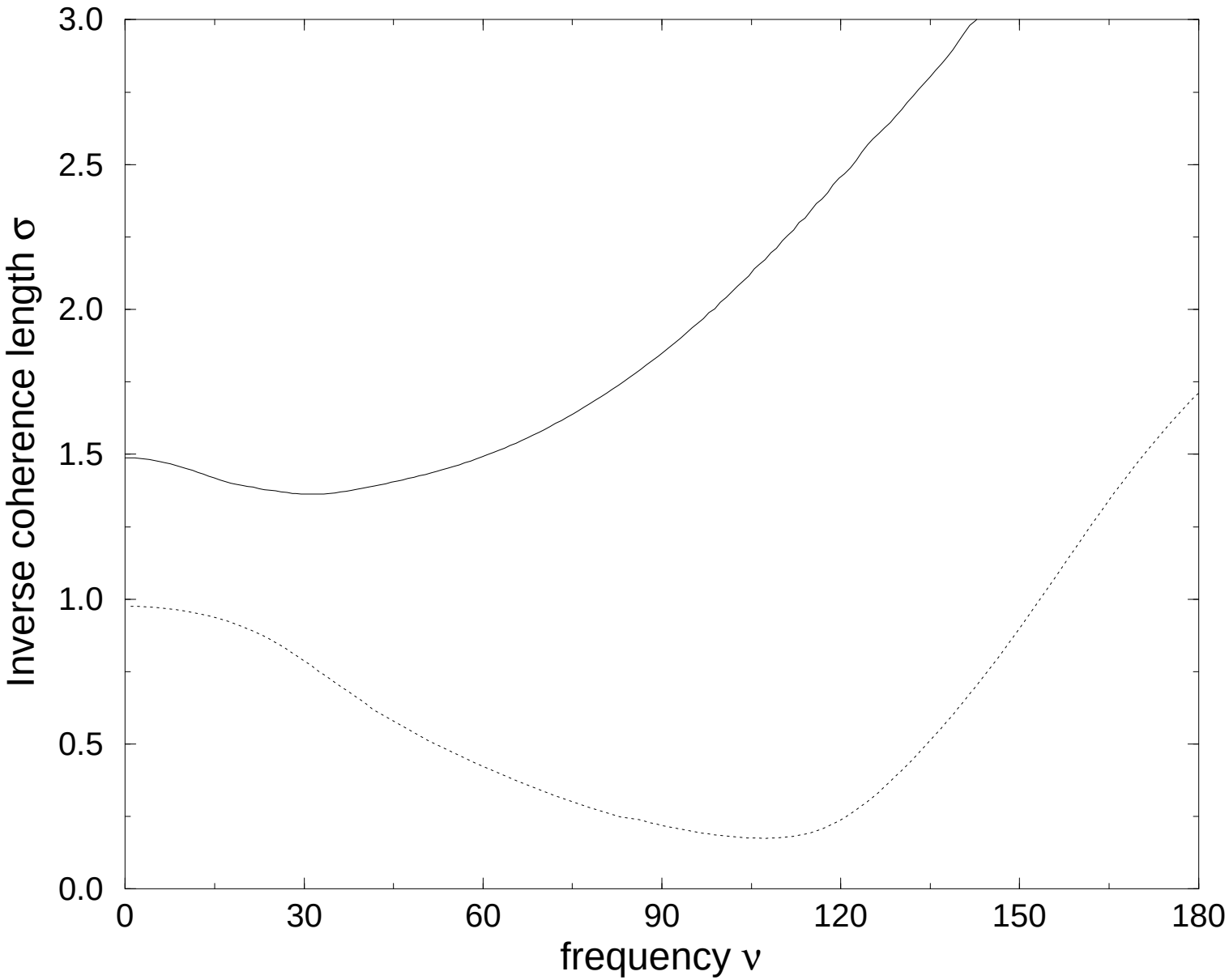
3.0
2.5
2.0
1.5
1.0
0.5
0.0
Inverse coherence length σ
0
30
60
90
120
150
180
frequency ν

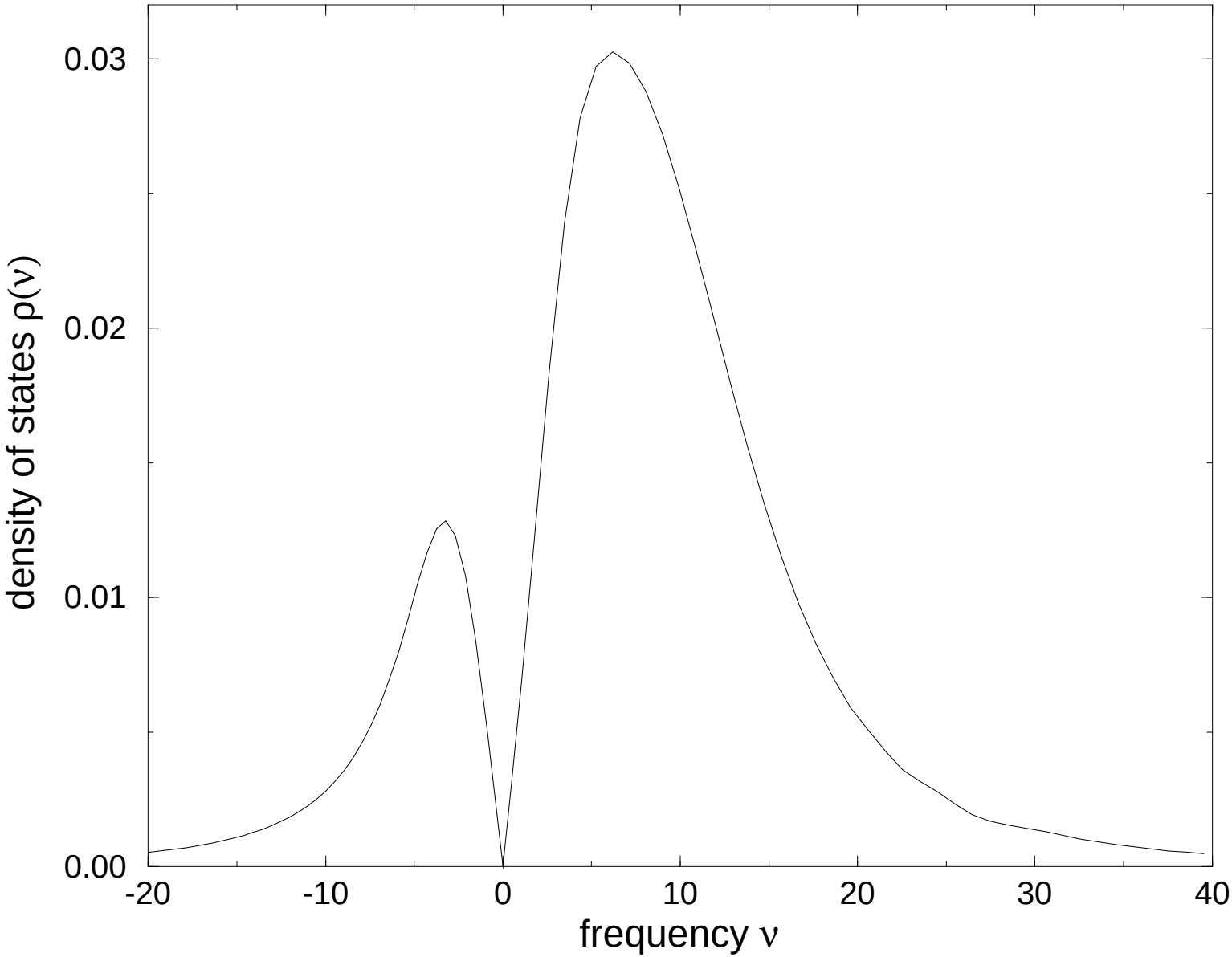
0.03
0.02
0.01
0.00
density of states ρ(ν)
-20
-10
0
10
20
30
40
frequency ν

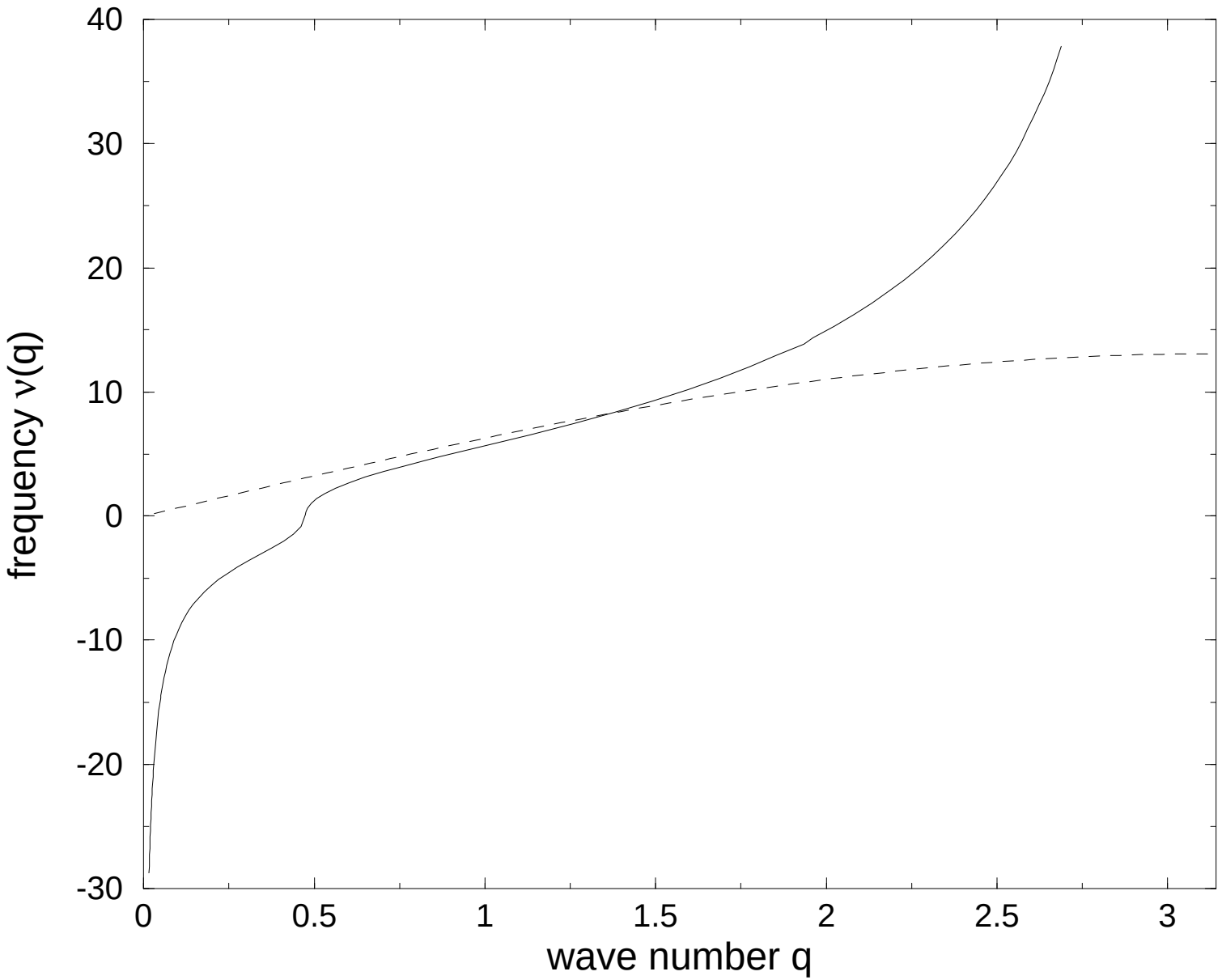
40
30
20
10
0
-10
-20
-30
0
0.5
1
1.5
2
2.5
3
frequency ν(q)
wave number q

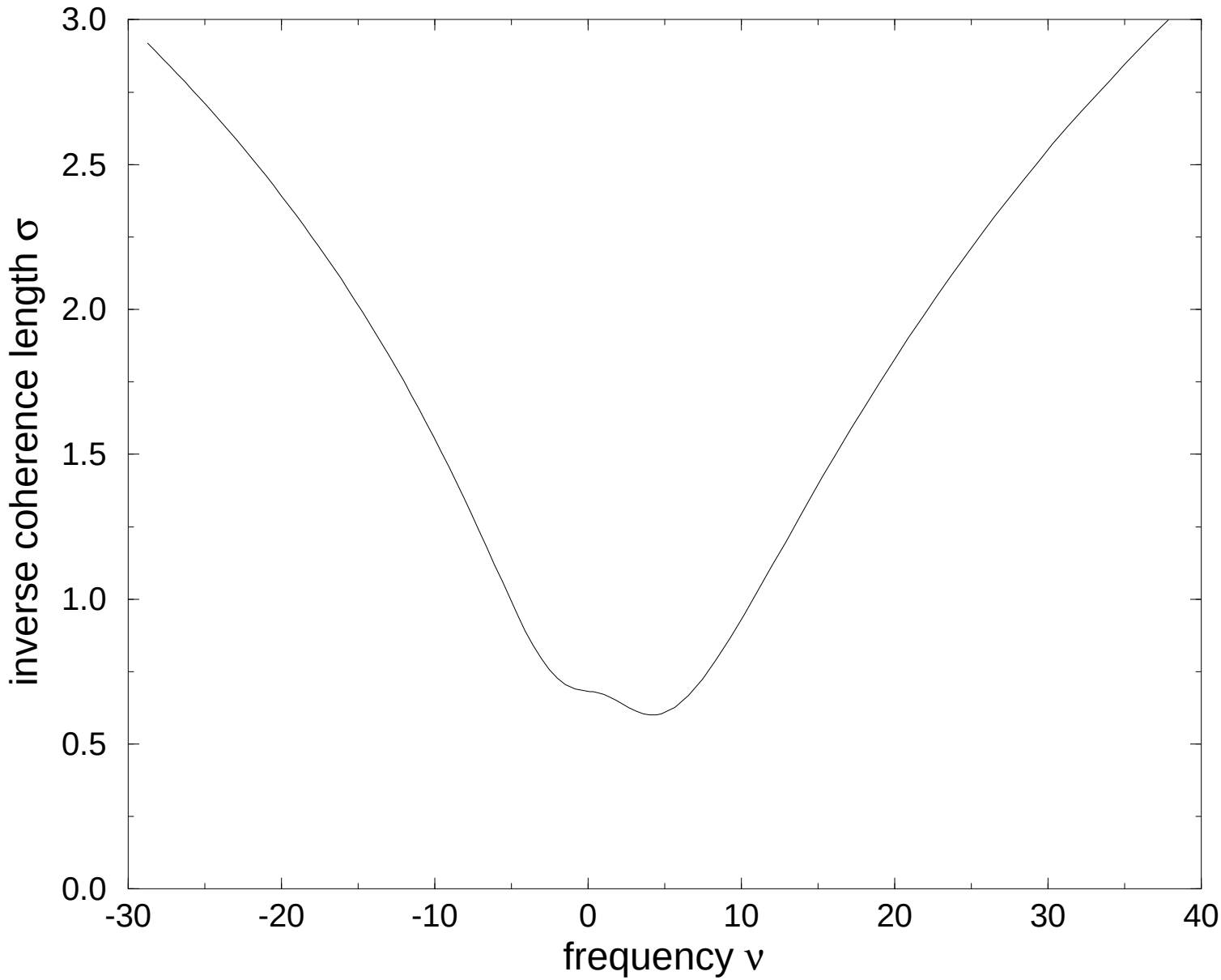
3.0
2.5
2.0
1.5
1.0
0.5
0.0
inverse coherence length σ
-30
-20
-10
0
10
20
30
40
frequency ν

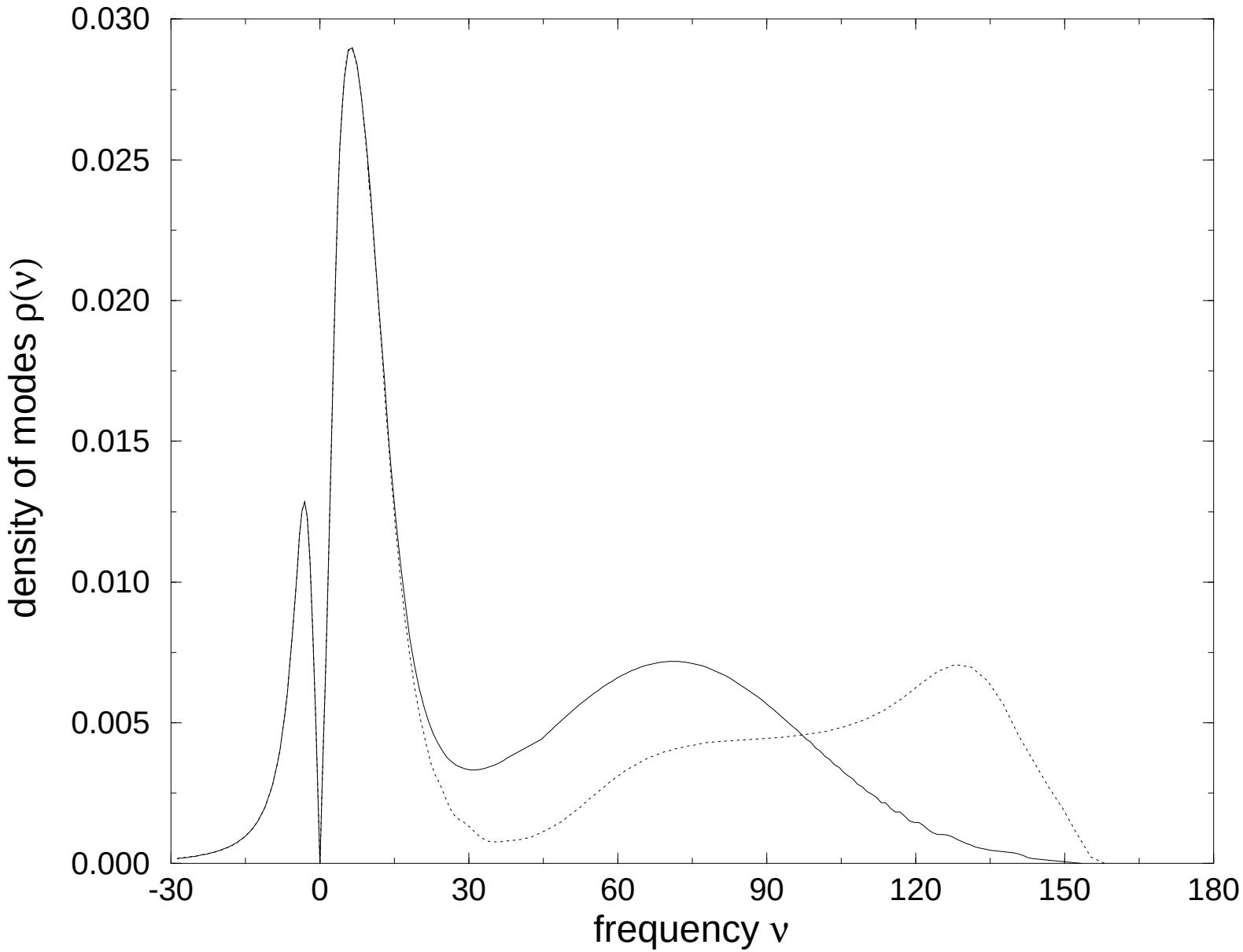
0.030
0.025
0.020
0.015
0.010
0.005
0.000
density of modes ρ(ν)
-30
0
30
60
90
120
150
180
frequency ν

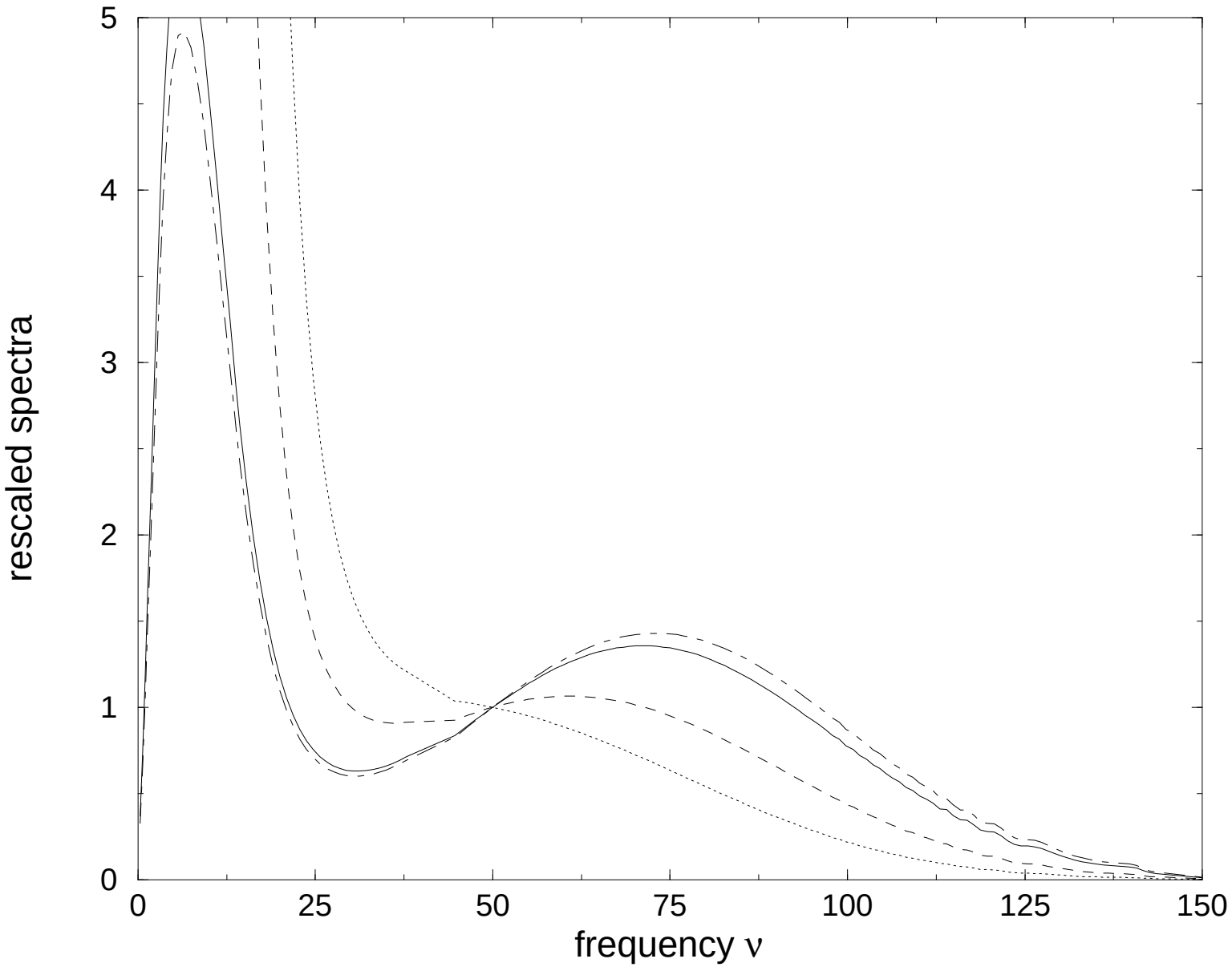
rescaled spectra
frequency ν
0
1
2
3
4
5
0
25
50
75
100
125
150

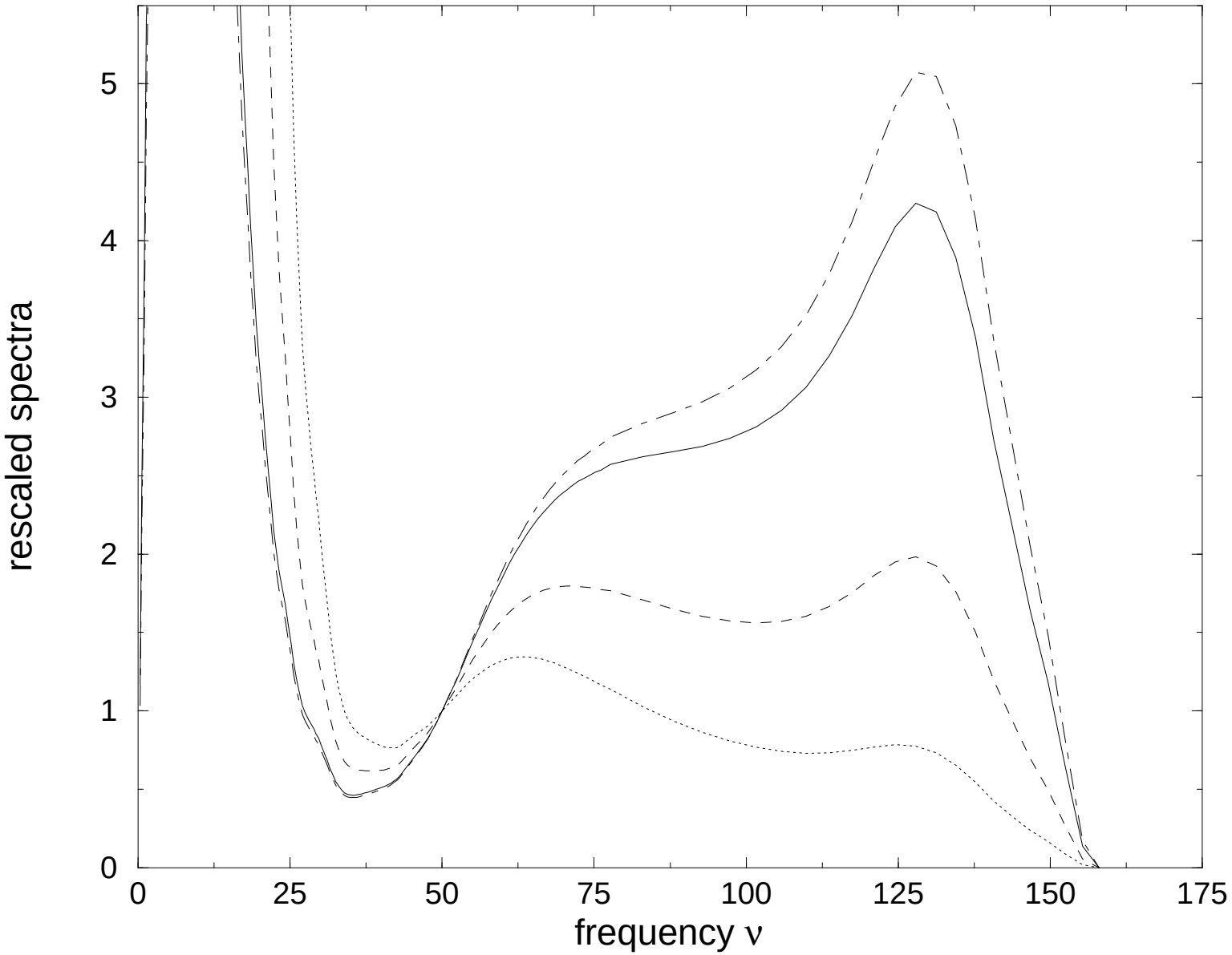
rescaled spectra
frequency ν
0
1
2
3
4
5
0
25
50
75
100
125
150
175